Observed impacts of aerosol concentration on maritime tropical convection within constrained environments using airborne radiometer, radar, lidar, and dropsondes

Corey G. Amiot[1,#], Timothy J. Lang[2], Susan C. van den Heever[3], Richard A. Ferrare[4], Ousmane O. Sy[5], Lawrence D. Carey[1], Sundar A. Christopher[1], John R. Mecikalski[1], Sean W. Freeman[3,##], George Alexander Sokolowsky[3,###], Chris A. Hostetler[4], and Simone Tanelli[5]

[1]Department of Atmospheric and Earth Science, The University of Alabama in Huntsville, Huntsville, AL, 35899, USA
[2]NASA Marshall Space Flight Center, Huntsville, AL, 35812, USA
[3]Department of Atmospheric Science, Colorado State University, Fort Collins, CO, 80523, USA
[4]NASA Langley Research Center, Hampton, VA, 23681, USA
[5]Jet Propulsion Laboratory, California Institute of Technology, Pasadena, CA, 91109, USA

[#]Now at NASA Postdoctoral Program, NASA Marshall Space Flight Center, Huntsville, AL, 35812, USA
[##]Now at Department of Atmospheric and Earth Science, The University of Alabama in Huntsville, Huntsville, AL, 35899, USA
[###]Now at Verisk Analytics, Inc., Boston, MA, 02111, USA

Correspondence to: Corey G. Amiot (corey.g.amiot@nasa.gov)

Abstract. Aerosol modulation of atmospheric convection remains an important topic in ongoing research. A key challenge in evaluating aerosol impacts on cumulus convection is isolating their effects from environmental influences. This work investigates aerosol effects on maritime tropical convection using airborne observations from NASA's Cloud, Aerosol and Monsoon Processes Philippines Experiment (CAMP^{2}Ex). Nine environmental parameters with known physical connections to cloud and storm formation were identified from dropsonde data, and 92 dropsondes were matched with corresponding CAMP^{2}Ex flight "scenes." To constrain environmental conditions, scenes were binned based on their association with "low," "medium," or "high" values for each dropsonde-derived parameter. In each scene and environmental bin, eight radar- and radiometer-based parameters directly related to convective intensity and/or prevalence were correlated with lidar-derived aerosol concentrations to examine trends in convective characteristics under different aerosol conditions. Threshold values used to stratify the environments were varied across four sensitivity tests to examine how the convective-aerosol correlations within each environmental bin responded. While results were mixed, some trends identified in the convective-aerosol analyses support the idea of warm-phase convective invigoration. General trends suggested that higher aerosol concentrations were correlated with stronger and/or more-prevalent convection in some cases, while other cases saw a "Goldilocks" zone of medium aerosol concentration favoring enhanced convection. These results indicate that medium-to-high aerosol concentrations may enhance convection, but these correlation analyses warrant further analysis, and our results stress the importance of considering environmental conditions when evaluating aerosol impacts.

Short summary

Decoupling aerosol and environmental impacts on convection is challenging. Using airborne data, we correlated convective metrics with aerosol concentrations in several different environments. Medium-to-high aerosol concentrations were occasionally strongly and positively correlated with convective intensity and prevalence, especially in favorable environments and cases with relatively high moisture near the surface. Storm environment is important to consider when evaluating aerosol effects.

1. Purpose and background

The primary purpose of this study is to explore potential impacts of aerosol concentration on maritime tropical convection during NASA's Cloud, Aerosol and Monsoon Processes Philippines Experiment (CAMP^{2}Ex) from a remote-sensing perspective within environmental contexts. The field phase of CAMP^{2}Ex occurred from 20 August – 10 October 2019, with instruments on NASA's P-3B Orion (P-3) aircraft sampling a wide range of environmental, cloud, radiation, and aerosol conditions across 19 research science flights (SFs) conducted out of Clark International Airport (Reid et al., 2023). The P-3 overflew a variety of cloud types during CAMP^{2}Ex, ranging in depth from shallow convection to deeper cumulus congestus and ranging in organization from isolated clouds to squall lines (Reid et al., 2023). Key instruments for this study that were flown on the P-3 during CAMP^{2}Ex include: the Advanced Microwave Precipitation Radiometer (AMPR; Spencer et al., 1994; Amiot et al., 2021), Airborne Precipitation and cloud Radar 3rd Generation (APR-3; Durden et al., 2020), High Spectral Resolution Lidar 2 (HSRL2; Burton et al., 2016), and Advanced Vertical Atmospheric Profiling System (AVAPS; Hock and Young, 2017). This research falls under the CAMP^{2}Ex science question of "To what extent are aerosol particles responsible for modulating warm and mixed-phase precipitation in tropical environments?", while also having direct implications for impacts on deeper convection and cloud meteorology (ESPO, 2020; Reid et al., 2023). A secondary purpose of this study is to expand and demonstrate the scientific utility of AMPR's geophysical retrievals (Amiot, 2023).

Aerosol impacts on convective storms have been a significant research topic. Increased aerosol concentration is generally associated with increased cloud condensation nuclei (CCN), with aerosol size distribution influencing cloud particle size distribution (Junge and McLaren, 1971). In shallow clouds, the second indirect effect of aerosols favors a decrease in precipitation formation and increase in cloud lifetime (Albrecht, 1989), resulting from reduced cloud droplet sizes due to increased competition for water vapor (e.g., Rosenfeld and Lensky, 1998; Sherwood, 2002). However, precipitation-sized hydrometeors that form in higher aerosol concentrations are generally larger, owing to ample cloud droplets available for collection and droplet growth (e.g., Stroud et al., 2007; Altaratz et al., 2008; Saleeby et al., 2010).

Many numerical-modeling studies have explored aerosol warm-phase invigoration in tropical convection. Sheffield et al., (2015) demonstrated how enhanced aerosol concentrations can increase cloud water content and produce more-vigorous updrafts via latent heat of condensation. Likewise, Marinescu et al., (2021) noted a 5–15% increase in mean updraft velocity around 4–7 km AGL when CCN concentrations were relatively high. Smaller cloud droplets

associated with higher aerosol concentrations may also enhance updraft/convective intensity via increased latent heat released during freezing and enhanced depositional growth above the environmental 0 °C level (e.g., van den Heever and Cotton, 2007; Rosenfeld et al., 2008). However, convective intensity increases are primarily driven by low-level condensational heating, rather than freezing above the environmental 0 °C level (Igel and van den Heever, 2021; Cotton and Walko, 2021), further indicating the importance of evaluating aerosol concentrations within/around warm-phase regions. Numerous other modeling studies have also demonstrated increased aerosol concentrations enhancing convection (e.g., van den Heever et al., 2006).

Several observational studies have also explored the impacts of increased aerosol concentrations on convection. For example, Lin et al., (2006) found enhancements in cloud height and cloud cover associated with increased aerosol concentrations in the Amazon. Likewise, Fan et al., (2018) identified increases in convective strength owing to the activation of additional CCN in regions with high concentrations of ultrafine aerosols in the Amazon. Using a combination of observations and simulations, Zhang et al., (2023) described how fine aerosols enhance convection which, in turn, modulates the surrounding environment and feeds back into larger-scale atmospheric circulations.

In contrast, many other studies (e.g., Grabowski and Morrison, 2016; Grabowski and Morrison, 2020; Varble, 2023) have presented evidence that increased aerosol concentrations do not invigorate convection above the environmental freezing level but may do so below the environmental freezing level. The former results from increased positive buoyancy, via enhanced latent heat of freezing, being offset by increased negative buoyancy, via mass loading from a greater liquid water content being lofted above the environmental freezing level (Grabowski and Morrison, 2020). The latter results from higher aerosol concentrations leading to lower supersaturation values within the surrounding environment and increased buoyancy, which in turn lead to higher updraft velocities and enhanced latent heating associated with increased condensation (e.g., Grabowski and Morrison, 2017; Grabowski and Morrison, 2020). Therefore, the role of enhanced aerosol concentration on updraft velocity can strongly depend on whether they are within regions wherein warm-phase or cold-phase processes dominate.

Similarly, despite numerous studies supporting the idea of convective enhancement from increased aerosol concentrations, many other studies have identified situations where higher aerosol concentrations may be detrimental for convection. For instance, entrainment of relatively dry environmental air may cause rapid evaporation of smaller cloud droplets associated with higher aerosol concentrations, decreasing cloud/storm structure (e.g., Liu et al., 2016). Veals et al., (2022) noted a tendency for weaker convection in the presence of higher aerosol concentrations in central Argentina. This raises several questions about the true impact of increased aerosol concentrations on convection, which motivates our study herein. These differences in the outcomes of past studies also indicate that a “Goldilocks” zone of medium aerosol concentration may favor the strongest convection (e.g., Sokolowsky et al., 2022). Further, other research discussed considerable difficulty in separating aerosol influences from atmospheric dynamics (e.g., Grabowski, 2018). Limitations in past numerical and observational studies are summarized by Varble et al., (2023), which highlights the continued uncertainty surrounding aerosol impacts on convection and motivates our study herein.

One remote-sensing instrument employed in aerosol analyses is lidar, including the High Spectral Resolution Lidar 2 (HSRL2) that was deployed on NASA's P-3 aircraft during CAMP^{2}Ex (Hostetler, 2020; Reid et al., 2023; Ferrare et al., 2023). HSRL2 measures aerosol backscatter and depolarization ratio at 355, 532, and 1064 nm, with aerosol extinction and aerosol optical thickness (AOT) also measured using the HSRL2 technique at 355 and 532 nm (Hostetler, 2020). Integration for calculating AOT occurs over a vertical distance starting near the surface and ending at the top of the aerosol extinction profile, which is often around 5–6 km AGL. Lenhardt et al., (2022) demonstrated how HSRL2's extinction and backscatter coefficients, especially at 532 nm, have strong direct correlations with CCN concentrations. Additional studies (e.g., Liu et al., 2016) noted a direct correlation between lidar-based AOT and CCN concentration. Therefore, extinction, backscatter, and AOT may all be considered when examining aerosol concentration. However, the height/location of an aerosol layer, which can be obtained from extinction and/or backscatter, is important to consider when evaluating diabatic heating from radiation absorption (e.g., Chand et al., 2009; Redemann et al., 2021). We will discuss HSRL2 data in more detail in section 2.

Based on these studies, the primary science question we address is: How do radiometer- and radar-based metrics of storm intensity and prevalence vary with lidar-based observations of aerosol concentration when binned into similar environmental groups throughout CAMP^{2}Ex? The results of these analyses are important as they provide insight into science questions for a major NASA field campaign, have relevance to upcoming NASA missions [e.g., Atmosphere Observing System (AOS, 2022)], and contribute knowledge to long-standing questions of aerosol influences on convection. We hypothesized that integrated cloud liquid water path (CLW), peak equivalent radar reflectivity factor (Z_H), peak Ku-/Ka-band radar dual-frequency ratio (DFR), and abundance of Z_H observations ≥ 30 dBZ in a given scene would all increase under higher aerosol concentrations within an environmental group. These hypotheses were based on expectations that increased aerosol concentrations would favor development of smaller and more-numerous cloud droplets, enhancing convection and CLW, while the presence of fewer but larger raindrops would increase maximum Z_H and overall presence of $Z_H \geq 30$ dBZ along with greater Ka-band attenuation compared to Ku band (i.e., increased maximum DFR). Further, we hypothesized that radar- and radiometer-based metrics of storm intensity and prevalence would all increase under greater 700-hPa w, CAPE, K-Index, LRs, and low-level T_d, though this investigation is secondary to our aerosol analyses in this study. Expectations for LCL altitude were more uncertain; some studies (e.g., Mulholland et al., 2021) have discussed the tendency for higher LCL altitude to favor stronger updrafts, but other studies (e.g., Grabowski, 2023) have presented alternate explanations, and greater low-level water vapor content would be associated with a lower LCL altitude. Thus, the influence of LCL altitude on convective intensity is still debated in the literature. Given the environmental stratification methods employed, as discussed in the next section, our focus was primarily on the correlations between convective and aerosol metrics and secondarily on the convective patterns associated with environmental variations, as mentioned previously. However, in each of these analyses, it is essential to note that correlation does not necessarily indicate causality, as a correlation between two variables may exist entirely due to indirect effects (e.g., Kretschmer et al., 2017). In addition, it must be acknowledged that these radar- and radiometer-based metrics of convective intensity may vary due to factors not specifically owing to changes in peak updraft intensity (e.g., cloud microphysics; e.g., Varble et al., 2023). Despite

these and other inherent difficulties, limitations, and uncertainties associated with separating aerosol and environmental influences on convection (e.g., Grabowski, 2018), potential trends found in the CAMP^{2}Ex dataset could provide useful information to support future work. Section 2 covers the data and methods used, with Sects. 3 and 4 highlighting environmental stratification and aerosol analyses from the microwave-frequency datasets. Section 5 presents a summary, discussion of limitations, and future work.

2. Data and analysis methods

All AMPR, APR-3, AVAPS, and HSRL2 data were gathered from the CAMP^{2}Ex data repository (Aknan and Chen, 2020). Due to the direct correlations between CCN concentration and lidar extinction, backscatter, and AOT, all three parameters were analyzed from HSRL2's 355- and 532-nm channels that employ the HSRL2 technique, though 532-nm backscatter was of particular interest based on discussions in Lenhardt et al., (2022). The same quality control (QC) processes outlined in Amiot (2023) for the AMPR, APR-3, and AVAPS data were applied for this study, including application of AMPR's multiple data quality flags and removal of the same 10 APR-3 files and 10 AVAPS dropsondes. Starting with the initial 144 dropsondes examined in Amiot (2023), a test was performed to determine whether each dropsonde passed through cloud. Given the 3% uncertainty in AVAPS RH (Freeman et al., 2020), any dropsonde where more than 20% of the dropsonde profile was associated with RH > 97% was removed from the analysis, which amounted to five dropsondes in total. The HSRL2 data were screened for clouds (Hostetler, 2020) to avoid potential contamination of the aerosol analyses (e.g., Liu et al., 2016). Uncertainty values associated with each instrument were deemed negligible for this study. More specifically, AMPR's root-mean-square deviation and median absolute deviation are both on the order of 10^{-2} kg m^{-2} (Amiot, 2023) and AMPR's noise-equivalent differential temperature (NEDT) is 0.5–1.0 K (Amiot et al., 2021). APR-3's Ku-band (Ka-band) calibration uncertainty is roughly 1 dB (1.5 dB) (Durden et al., 2020). The uncertainties in AVAPS's temperature, relative humidity, and pressure measurements are 0.2 °C, 3%, and 0.5 hPa, respectively (Freeman et al., 2020). Systematic errors for HSRL2 are approximately 4.7% (5.0%) for the 355-nm (532-nm) channel (Burton et al, 2015). Nine environmental parameters with known physical connections to convective intensity were subjectively chosen for this study based on their ability to be fully captured by a statistically significant number of CAMP^{2}Ex dropsondes; future work would benefit from examining other environmental conditions. The nine selected parameters were: 700-hPa w; *modified* CAPE; LCL altitude; K-Index; 850–700-, 850–500-, and 700–500-hPa LRs; mean T_d below the 925-hPa level; and mean T_d below 1 km AGL, hereafter referred to by their symbols in Table 1.

A significant challenge in evaluating aerosol impacts on convection is to isolate aerosol influences from other sources of convection modulation, such as atmospheric dynamics, thermodynamics, and cloud microphysical processes (e.g., Liu et al., 2016; Grabowski 2018). Since a given convective plume will be affected by synoptic-scale (> 2000 km), mesoscale (2–2000 km), and sub-mesoscale (< 2 km) dynamics (Orlanski, 1975) and environmental conditions, it is important to understand and constrain environmental conditions associated with any convective element (herein "storm") of interest. Several environmental factors with direct physical connections to convection can be evaluated from remote-sensing and in situ observation platforms. Studies have demonstrated the utility of radiosonde data, the

Table 1: List of symbols used to represent the environmental, convective, and aerosol variables examined in this study, along with their units and a brief description of each variable.

Symbol	Units	Type	Description
w_{700}	m s^{-1}	Environmental	Vertical velocity at 700-hPa level
$NCAPE_{mod}$	m s^{-2}	Environmental	Modified Normalized Convective Available Potential Energy
LCL	m	Environmental	Lifting Condensation Level altitude
K-Index	°C	Environmental	K-Index value
$LR_{850\text{-}700}$	°C km^{-1}	Environmental	Temperature lapse rate between 850- and 700-hPa levels
$LR_{850\text{-}500}$	°C km^{-1}	Environmental	Temperature lapse rate between 850- and 500-hPa levels
$LR_{700\text{-}500}$	°C km^{-1}	Environmental	Temperature lapse rate between 700- and 500-hPa levels
$T_{d,press}$	°C	Environmental	Mean dew point temperature below 925-hPa level
$T_{d,alt}$	°C	Environmental	Mean dew point temperature below 1 km AGL
CLW	kg m^{-2}	Convective	AMPR-derived columnar cloud liquid water path
PCT_{10}	K	Convective	AMPR 10.7-GHz polarization-corrected temperature
PCT_{19}	K	Convective	AMPR 19.35-GHz polarization-corrected temperature
PCT_{37}	K	Convective	AMPR 37.1-GHz polarization-corrected temperature
PCT_{85}	K	Convective	AMPR 85.5-GHz polarization-corrected temperature
$Z_{95,Ku}$	dBZ	Convective	APR-3 Ku-band 95th percentile composite reflectivity
$Pixels_{Ku}$	unitless	Convective	APR-3 Ku-band composite reflectivity pixels ≥ 30 dBZ
DFR	unitless	Convective	APR-3 Ku-/Ka-band dual-frequency ratio
AOT_{355}	unitless	Aerosol	HSRL2 355-nm aerosol optical thickness
AOT_{532}	unitless	Aerosol	HSRL2 532-nm aerosol optical thickness
Ext_{355}	Mm^{-1}	Aerosol	HSRL2 355-nm aerosol extinction
Ext_{532}	Mm^{-1}	Aerosol	HSRL2 532-nm aerosol extinction
Bsc_{355}	Mm^{-1} sr^{-1}	Aerosol	HSRL2 355-nm aerosol backscatter
Bsc_{532}	Mm^{-1} sr^{-1}	Aerosol	HSRL2 532-nm aerosol backscatter

principles of which can be applied to dropsondes (e.g., AVAPS) to the extent offered by the dropsonde's launch altitude. Vertical velocity (w) at the 700-hPa level can be used to diagnose vertical motion and associated convective support (Bony et al., 2004; Liu et al., 2016). Convective Available Potential Energy (CAPE), a measure of parcel buoyancy that is used to diagnose potential updraft velocity, is defined via

$$\text{CAPE}\left(\text{J kg}^{-1}\right) = g\int_{z_{lfc}}^{z_{el}} \frac{\left(T_v - T_{v,0}\right)}{T_{v,0}}\, dz, \tag{1}$$

where g is gravitational acceleration; T_v and $T_{v,0}$ are parcel and environmental virtual temperatures, respectively; z is altitude; and z_{lfc} and z_{el} altitudes of the level of free convection and equilibrium level, respectively (Markowski and Richardson, 2010).

The Lifting Condensation Level (LCL) altitude indicates cloud-base height and is often used in forecasting convection (Markowski and Richardson, 2010), though the exact role of LCL altitude on convective intensity is debated in the

literature (e.g., Mulholland et al., 2021; Grabowski, 2023). K-Index is used to forecast convective potential/prevalence (i.e., not intensity) and is defined as

$$\text{K-Index}(°\text{C}) = (T_{850} - T_{500}) + T_{d,850} - (T_{700} - T_{d,700}) \quad (2)$$

where T_{850}, T_{700}, and T_{500} are temperatures at the 850-, 700-, and 500-hPa levels, respectively, and $T_{d,850}$ and $T_{d,700}$ are dew point temperatures at the 850- and 700-hPa levels, respectively (George, 1960). From Eq. (2), K-Index considers: 1) low-to-mid-level temperature lapse rate (hereafter simply "lapse rate", LR), 2) low-level dew point temperature (T_d), and 3) mid-level T_d depression, with the former two (latter one) being directly (inversely) related to convective potential. In addition to 850–500-hPa, 700–500-hPa LR may serve as an excellent indicator of convective potential (e.g., Sherburn and Parker, 2014). Others (e.g., Wang et al., 2015) have used 850–700-hPa LR in forecasting convective potential due to its association with parcel vertical acceleration in the lower atmosphere. Lastly, low-level T_d is important for convective intensity ("intensity" referring to peak updraft velocity) due to entrainment of relatively high-water-vapor air into an updraft's base (e.g., Lucas et al., 2000).

We utilize microwave remote-sensing signatures from radar and radiometer to evaluate convective intensity and prevalence. The 30-dBZ Z_H isoline has often been used to identify precipitation regions (e.g., Straka et al., 2000) and delineate between different "storms" or "cells" (e.g., Johnson et al., 1998; Hastings and Richardson, 2016; Amiot et al., 2019). As precipitation-sized hydrometeors form and grow, Z_H increases due to hydrometeor diameter (D) weighting of D^6 associated with Rayleigh scattering, with eventual onset of non-Rayleigh resonance effects for larger values of D relative to the radar wavelength (Rinehart, 2010). This is especially important to note at finer wavelengths, such as 2.2 and 0.84 cm associated with the Airborne Precipitation and cloud Radar 3rd generation (APR-3)'s Ku and Ka bands, respectively (Durden et al., 2020), the primary radar dataset used herein. A combination of Ku- and Ka-band radar can be powerful when evaluated using dual-frequency ratio (DFR):

$$\text{DFR} = Z_{Ku} - Z_{Ka}, \quad (3)$$

where Z_{Ku} and Z_{Ka} represent Z_H at Ku- and Ka-band, respectively, on a logarithmic scale (i.e., expressed in dBZ) (e.g., Liao et al., 2008; Liao and Meneghini, 2011). In regions where Z_{Ku} and Z_{Ka} are both similar (e.g., near 0 dBZ for hydrometeors that are in the Rayleigh scattering regime at both frequencies), DFR will be near zero; however, departures in DFR from 0 dBZ can indicate differences in attenuation between the two frequencies and can be used to infer hydrometeor size and phase (e.g., Liao and Meneghini, 2011). As Ku-band Z_H increases, the DFR in rain regions generally becomes slightly negative (i.e., -1–0) before increasing to positive values for $Z_H > 30$ dBZ; in regions of ice hydrometeors, DFR generally increases with increasing Ku-band Z_H, with a steeper increase occurring for lower-density ice hydrometeors (Liao and Meneghini, 2011).

Microwave radiometers generally retrieve higher brightness temperature (T_b) values at increasingly lower frequencies as precipitation hydrometeors grow in the absence of ice formation aloft (e.g., Spencer et al., 1994). This makes it possible to retrieve cloud and precipitation properties using T_b combinations (e.g., Wilheit and Chang, 1980; Wentz and Spencer, 1998; Hong and Shin, 2013; Amiot et al., 2021). AMPR's integrated cloud liquid water path (CLW) retrievals often fail within precipitation regions; thus, as a cloud grows vertically, AMPR-derived CLW is expected

to increase until it fails in moderate-to-heavy precipitation (Amiot et al., 2021; Amiot, 2023). However, CLW increasing around precipitation may yield useful information about the associated convective intensity; for example, precipitation is often associated with cumulus clouds at least 1.5–2 km tall (Smalley and Rapp, 2020) and CLW > 1 kg m^{-2} may indicate precipitation formation within these clouds (e.g., Jiang and Zipser, 2006).

Vertical ascent is a parameter included within the AVAPS dataset (Vömel et al., 2020) and is based on the fall-speed characteristics of the dropsonde (Freeman et al., 2020). The ascent value from the pressure array element nearest 700 hPa was used as w_{700}. Since CAPE is related to integrated buoyancy between the LFC and EL via Eq. (1), an issue arises with computing CAPE from AVAPS during CAMP^{2}Ex; since the P-3 did not fly above the EL during any science flight (SF), the dropsondes did not capture the full vertical buoyancy profile associated with traditional CAPE. As such, the term "modified CAPE" is used herein and is defined mathematically as

$$\mathrm{CAPE}_{\mathrm{mod}}\left(\mathrm{J\ kg^{-1}}\right) = g\int_{z_{lfc}}^{z_{P3}} \frac{\left(T_v - T_{v,0}\right)}{T_{v,0}}\, dz, \tag{4}$$

where z_{P3} is the P-3 altitude and all other terms are the same as in Eq. (1). With this definition, modified CAPE would be less than true CAPE within the same environment, which limits evaluation of parcel buoyancy. Since the dropsondes were often launched when the P-3 altitude was > 4 km AGL (Vömel et al., 2020), the instability indicated by modified CAPE can be compared across the environments. Despite this, P-3 altitude would have a direct effect on modified CAPE calculated via Eq. (4), with lower altitude (e.g., around 4 km AGL) biased toward lower modified CAPE by virtue of the dropsonde capturing a lesser vertical extent of the parcel buoyancy. To mitigate this effect, we normalized the CAPE via dividing by the dropsonde launch altitude, which yields (modified) normalized CAPE (Blanchard, 1998) via the relation

$$\mathrm{NCAPE}_{\mathrm{mod}}\ (\mathrm{m\ s^{-2}}) = \frac{\mathrm{CAPE}_{\mathrm{mod}}}{\mathrm{z}}, \tag{5}$$

where z is dropsonde launch altitude. In addition to normalizing the CAPE profiles by dropsonde launch altitude, an added benefit of examining $\mathrm{NCAPE}_{\mathrm{mod}}$ is that its units are m s^{-2}, allowing direct examination of vertical acceleration over the dropsonde layer (Blanchard, 1998). All CAPE and LCL values were calculated using functions within the Python programming language (i.e., May et al., 2022) as noted in the data availability statement.

K-Index was calculated semi-manually by identifying the pressure array elements nearest the 850-, 700-, and 500-hPa levels, extracting the associated T and/or T_d values from these elements, and utilizing Eq. (2). In a similar manner, the temperature and altitude values from array elements nearest the 850-, 700-, and 500-hPa levels were used to calculate $\mathrm{LR}_{850\text{-}700}$, $\mathrm{LR}_{850\text{-}500}$, and $\mathrm{LR}_{700\text{-}500}$ as

$$\mathrm{LR}\left(^{\circ}\mathrm{C\ km^{-1}}\right) = -\frac{\left(T_{upper} - T_{lower}\right)}{\left(z_{upper} - z_{lower}\right)}, \tag{6}$$

where LR is lapse rate, T_{upper} and T_{lower} are temperatures at the higher and lower altitudes, respectively, and z_{upper} and z_{lower} are the higher and lower altitudes, respectively. Lastly, mean low-level T_d values were calculated by finding array elements where 1) pressure was > 925 hPa, or 2) altitude was < 1 km AGL, and calculating mean T_d from the associated array elements.

Once the above parameters were calculated from each dropsonde throughout CAMP^{2}Ex SFs 05–19, they were matched spatiotemporally with AMPR and APR-3 data. AMPR was inoperable during SF 01 and had un-optimized settings for its gain and offset values during SFs 02–04 (Lang et al., 2021), resulting in the exclusion of SFs 01–04 at the outset of our study. A "scene" was then established for each dropsonde, defined herein using a standard duration of 10 minutes calculated as ±5 minutes from the dropsonde launch time. To account for situations where remote-sensing data collection began shortly before or after the start and/or end time of a given scene (e.g., P-3 was turning at the calculated start or end time), a grace of ±1 minute was allowed for the total scene duration, yielding a 10% uncertainty in scene duration. Scenes where the calculated duration was < 9 or > 11 minutes were masked from the analysis, which amounted to 47 dropsondes in total. Out of the 144 initial dropsondes, five were removed due to the aforementioned RH analysis, and the removal of these 47 additional dropsondes yielded total of 92 dropsondes retained for our study. The AMPR, APR-3, and HSRL2 scans nearest the start and end times of each scene were noted, and all AMPR, APR-3, and HSRL2 data were examined over the same approximate time period within each scene; an example of these data in a single scene is provided in Fig. 1. Eight remote-sensing parameters related to convective intensity and/or prevalence were calculated in each scene: 95th percentile (p95) of AMPR CLW; p95 of AMPR polarization-corrected temperature (PCT) at 10.7, 19.35, 37.1, and 85.5 GHz; p95 of APR-3 Ku-band composite Z_H and DFR, and number of APR-3 Ku-band composite Z_H pixels ≥ 30 dBZ, hereafter referred to by their symbols in Table 1. The p95 values were used for the former seven parameters due to their direct association with peak convective intensity (e.g., increased raindrop size and radar reflectivity with stronger updraft, all else being equal; e.g., Kollias et al., 2001), with the 95th percentile employed to avoid potential outlier values associated with maximum values. Ku-band was used for the composite Z_H analyses given its reduced attenuation compared to a Ka-band signal over the same distance and atmospheric conditions (i.e., all else being equal). To calculate composite Z_H, the data QC described in Amiot (2023) was applied to all 25 APR-3 scan angles in each scene. Within each column of QC'd APR-3 data across SFs 05–19, the maximum Z_H between the P-3 altitude and the surface was used as the composite Z_H. The presence of occasional residual near-surface range-/sidelobe effects at off-nadir scan angles was noted, which often manifested as very high composite Z_H (i.e., > 70 dBZ). As a basic restriction, all composite Z_H pixels > 70 dBZ were excluded from our analyses, but some erroneous pixels may still reside in the final dataset (e.g., isolated cases with some noisy pixels and/or near-surface range-/sidelobe effects with Z_H < 70 dBZ). Once all composite Z_H values were calculated, $Z_{95,Ku}$, DFR, and $Pixels_{Ku}$ were recorded in each scene. AMPR PCT values were calculated following the methods of Cecil and Chronis (2018), with their methods for 89.0-GHz data applied directly to AMPR's 85.5-GHz data. The p95 PCT in each AMPR channel was recorded along with the p95 of retrieved AMPR CLW in each scene.

To begin isolating potential aerosol influences on tropical convection, two steps were employed: 1) bin the environmental scenes into different groups based on a particular AVAPS parameter and magnitude, and 2) incorporate HSRL2 data into this analysis. The nine AVAPS parameters listed in Table 1 were employed. To stratify each environment, a single AVAPS parameter was separated into "low," "medium," and "high" values, and each scene was grouped into one of these categories based on the associated dropsonde's values. Within each environmental bin, the

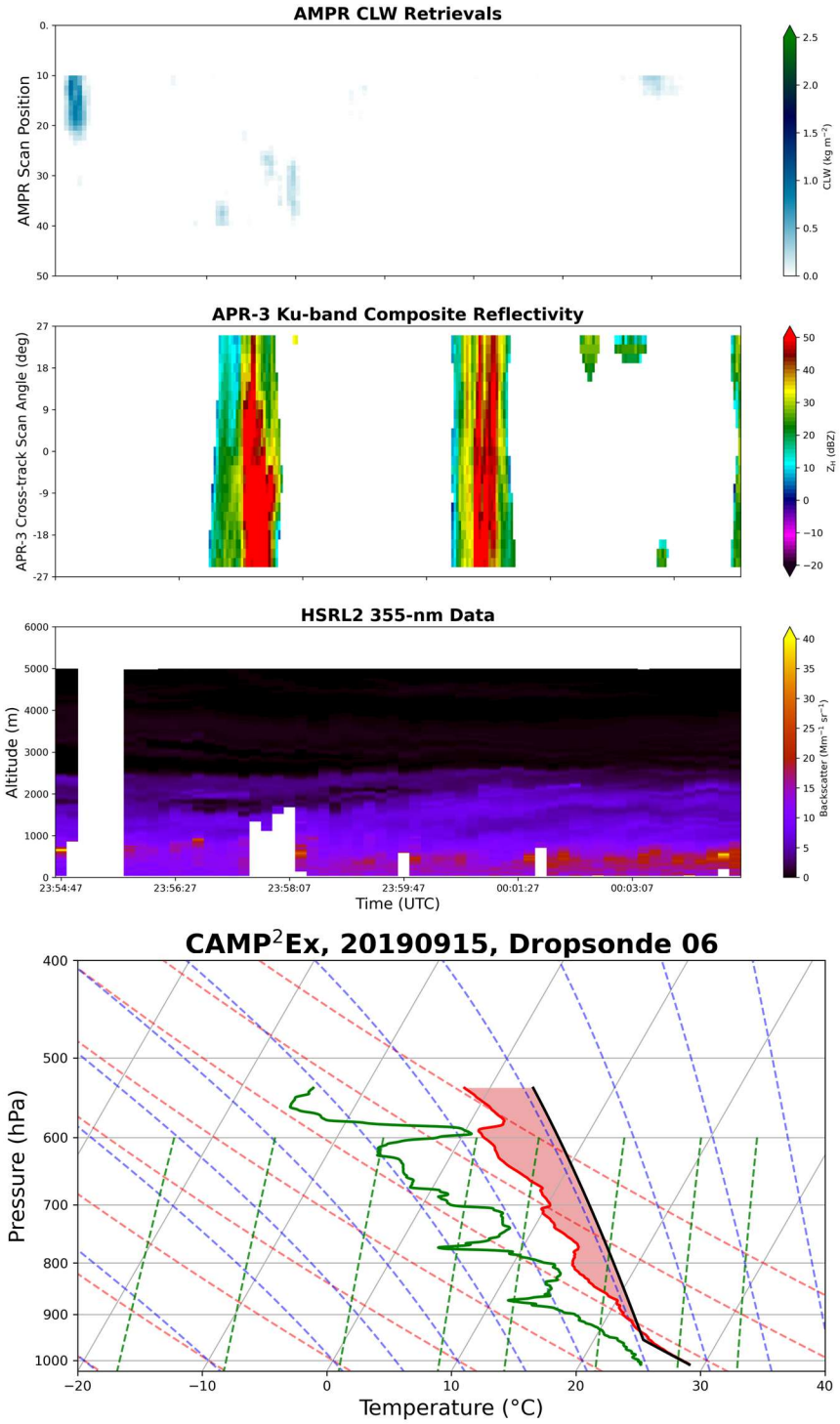

Figure 1: Strip charts (i.e., top-view time series) of AMPR CLW (top) and APR-3 Ku-band composite Z_H (second from top) along with a time-height plot of HSRL2 532-nm backscatter (second from bottom) from approximately 2354–0004 UTC during SF 09, which cover the "scene" associated with the dropsonde shown in the bottom panel. The dropsonde was launched at 2359:50 UTC. All AMPR data flags have been applied in the top panel. Red shading in the bottom panel indicates CAPE, while solid red, green, and black lines denote temperature, dew point temperature, and parcel temperature, respectively.

eight convective parameters were compared against mean values of the six HSRL2 parameters (Table 1) from each scene. The main statistics examined were Pearson correlation coefficients, the number of data points used in each comparison, and the statistical significance, primarily based on whether the p-value associated with the Pearson correlation coefficient was < 0.01 (e.g., Wilks, 2011). A few subjectively selected correlations were examined in greater detail using scatterplots, wherein it should be noted that the exact number of data points varied from plot-to-plot due to variations in missing data (e.g., dropsonde launched below the 500-hPa level for any parameters that use 500-hPa data). In addition, several scenes contained no unmasked APR-3 and/or AMPR data, resulting in their exclusion from the comparisons.

Lastly, the exact values used to stratify each environmental condition were varied in a sensitivity test consisting of four different sets of thresholds for each parameter (Table 2). The methods used to stratify the environmental parameters in Tests 1–4 were, respectively, as follows:

1) Create campaign-wide histograms of the AVAPS parameter and visually identify approximate values that split the dataset into three roughly equal-sized groups.
2) Objectively select thresholds that split each parameter's dataset into three equal-sized groups (see the Data Availability statement).
3) Manually select thresholds that fall between the low-medium and medium-high thresholds previously identified in Tests 1 and 2.
4) Objectively select thresholds that split each parameter's dataset into three groups where the "low" and "high" categories each contain 25% of the data and the "medium" category contains 50% of the data (i.e., "medium" datasets that were approximately twice as large as the "low" and "high" datasets).

For brevity, only results from Test 2 are shown herein, but results from all four tests can be found in supplemental material. Test 2 is highlighted due to its objective stratification into roughly equal-sized groups.

3. AMPR results

This section presents the results of comparing the AMPR-based convective parameters with HSRL2 data within environmental bins established using the nine AVAPS parameters. Correlation tables are used to provide complete descriptions of the observed correlations, with more in-depth discussions and analyses performed for some subjectively selected correlations that were statistically significant and/or potentially most impactful. A brief description of the sensitivity test results for environmental stratification is provided for each parameter, and all associated correlation tables from these sensitivity tests can be found in supplemental material.

AMPR's CLW comparisons with HSRL2 in the stratified environments are summarized in Fig. 2. From Fig. 2, many Pearson correlation coefficients between the aerosol parameters and CLW were negative and with statistical significance, especially when comparing CLW with AOT and Ext at either HSRL2 wavelength. This result was unexpected but, as will be elaborated upon further in this section, was primarily due to the masking of precipitation regions for AMPR CLW. Due to the CLW retrieval method not accounting for precipitation, regions wherein high

Table 2: List of the four sensitivity tests that were performed to stratify the nine AVAPS parameters into "low," "medium," and "high" bins. The listed values in each bracket represent the inclusive range of the "medium" bin for the respective parameter and test; that is, values less (greater) than the lower (upper) limit were classified into the "low" ("high") bin.

AVAPS parameters	Test 1: Visual histogram analysis	Test 2: Objective split 0.33-0.33-0.33	Test 3: Manual selection between Tests 1 and 2	Test 4: Objective split 0.25-0.50-0.25
$T_{d,alt}$	[21.0, 22.5] °C	[21.72, 22.4] °C	[21.35, 22.45] °C	[21.52, 22.59] °C
$T_{d,press}$	[22.0, 23.0] °C	[22.62, 23.2] °C	[22.3, 23.1] °C	[22.34, 23.39] °C
$LR_{700\text{-}500}$	[5.5, 6.0] °C km^{-1}	[5.52, 5.9] °C km^{-1}	[5.51, 5.95]°C km^{-1}	[5.39, 6.01] °C km^{-1}
$LR_{850\text{-}500}$	[5.0, 5.5] °C km^{-1}	[5.18, 5.43] °C km^{-1}	[5.1, 5.47] °C km^{-1}	[5.12, 5.46] °C km^{-1}
$LR_{850\text{-}700}$	[4.5, 5.5] °C km^{-1}	[4.25, 4.98] °C km^{-1}	[4.35, 5.25] °C km^{-1}	[4.06, 5.11] °C km^{-1}
K-Index	[30, 35] °C	[31.08, 35.61] °C	[30.5, 35.3] °C	[30.07, 36.59] °C
LCL	[400, 550] m	[404.1, 480.28] m	[402, 525] m	[369.36, 509.86] m
$NCAPE_{mod}$	[0.04, 0.06] m s^{-2}	[0.03, 0.05] m s^{-2}	[0.035, 0.055] m s^{-2}	[0.02, 0.06] m s^{-2}
w_{700}	[-0.25, 0.25] m s^{-1}	[-0.17, 0.06] m s^{-1}	[-0.20, 0.15] m s^{-1}	[-0.29, 0.12] m s^{-1}

CLW would be expected in association with heavy precipitation could easily appear as a region of failed retrieval or may return a high CLW value with an unknown uncertainty (Amiot et al., 2021). For this reason, precipitation was masked for the AMPR CLW retrievals. A similar trend across the HSRL2 parameters and environmental bins, albeit with different correlation values and changes in their statistical significances, was observed across the sensitivity tests performed (supplemental material).

To gain a more in-depth look at some correlations in Fig. 2, scatterplots were produced of CLW versus AOT_{355} when binned by $NCAPE_{mod}$ (Fig. 3a) and CLW versus Bsc_{532} when binned by $LR_{850\text{-}700}$ (Fig. 3b). These correlations were selected for scatterplot analysis based on their statistical significance in Fig. 2 while also presenting CLW comparisons with two different aerosol parameters and using two different environmental parameters for the binning. From Fig. 3a, negative correlations can be seen between CLW and AOT_{355} for each of the environmental bins, though the negative correlations are most pronounced (and most statistically significant) within the medium and high $NCAPE_{mod}$ groups. The values of AOT_{355} are relatively low (< 0.5) for the entire analysis, which limits variability in the aerosol concentrations, but we will discuss the trends relative to the AOT_{355} values present. A notable feature in Fig. 3a is the clustering of data points around CLW = 0 kg m^{-2}, which suggests that several of the scenes examined either did not contain clouds or they were masked from the analyses; these trends will be seen in other comparisons discussed for the AMPR and APR-3 convective metrics in this section and section 4. The clustering of these data points around CLW = 0 kg m^{-2} as AOT_{355} increases seems to have contributed to the negative correlations for each environmental group. It should also be noted that CLW values > 1 kg m^{-2} are excluded from Fig. 3a; a CLW threshold of 1 kg m^{-2} has been used in prior studies (e.g., Jiang and Zipser, 2006) to separate precipitating and non-precipitating clouds, indicating that precipitation scenes were largely successfully masked from Fig. 3a. If precipitating scenes were indeed masked under the presence of higher AOT_{355} and higher $NCAPE_{mod}$ (i.e., the clustering of these data points above an AOT_{355} of 0.2), it would suggest that convection was strong enough to produce precipitation under higher aerosol concentrations and higher $NCAPE_{mod}$; however, this is speculative and cannot be determined from Fig. 3a alone, but this idea will be revisited throughout sections 3 and 4. Additionally, as will be referred throughout these discussions,

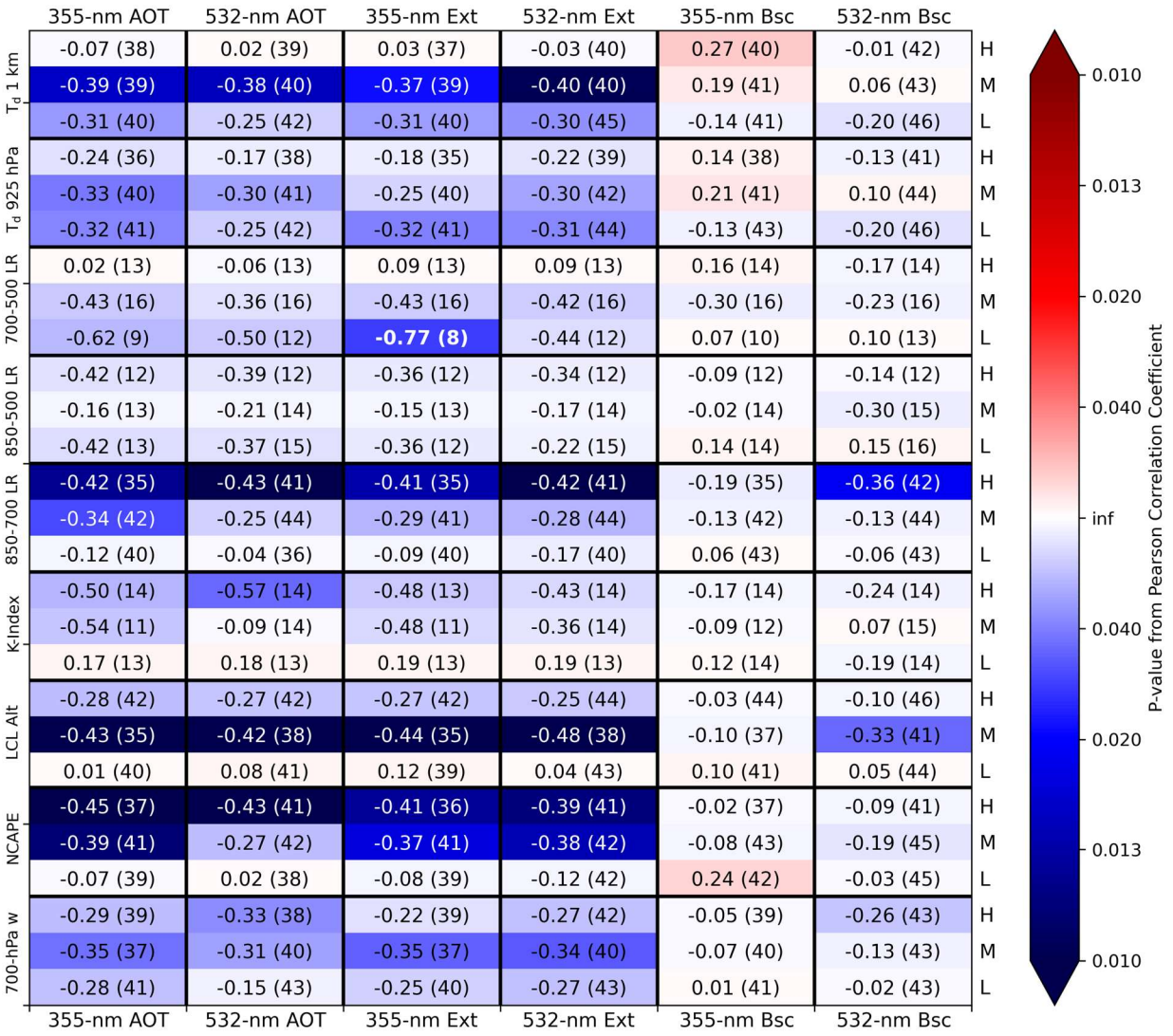

Figure 2: Pearson correlation coefficients from comparing p95 AMPR CLW with mean HSRL2 AOT, extinction (Ext), and backscatter (Bsc) at 355 and 532 nm (top and bottom borders) within environmental bins stratified by the nine AVAPS parameters (left border) at low (L), medium (M), and high (H) magnitudes (right border) across the CAMP^{2}Ex scenes. AVAPS magnitudes were stratified using the values of Test 2 (Table 2). Within each cell, the listed value is the Pearson correlation coefficient and the parenthesized value indicates the number of data points used in the comparison. Cells with a Pearson correlation coefficient ≥ 0.70 contain bolded text. Reds (blues) represent positive (negative) Pearson correlation coefficients, and the color shading corresponds to the magnitude of the p-value according to the colorbar, with darker shades of each color associated with lower p-values (i.e., greater statistical significance). Color shading begins to increase substantially around a p-value of 0.05 and reaches a maximum for p-values around 0.01.

a relatively limited sample size was present for several of the comparisons/scatterplots, and all cases examined in this study would benefit greatly from a larger sample. Despite this, the statistical significance between CLW and AOT_{355} is potentially impactful and warrants further investigation.

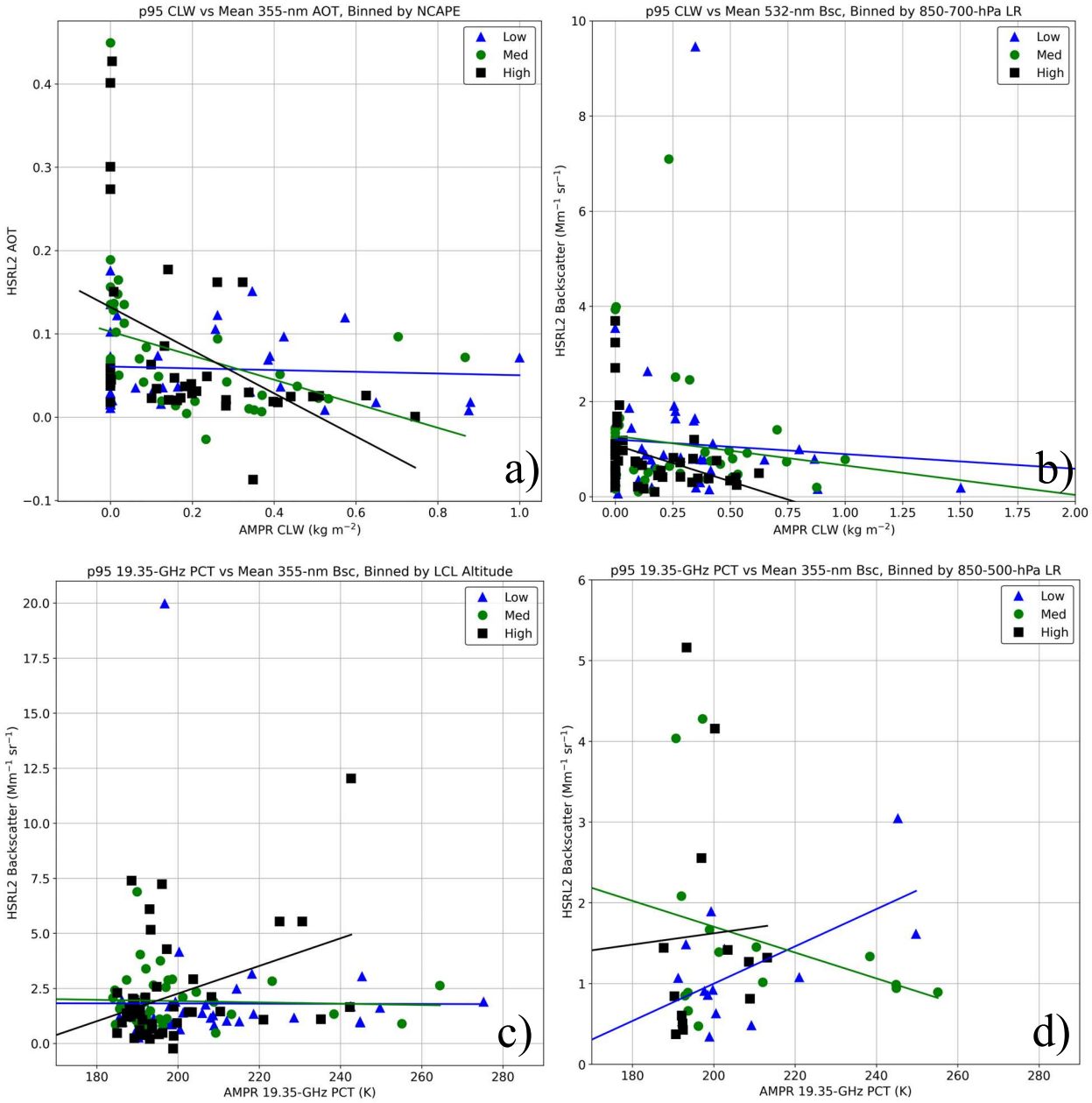

Figure 3: Scatterplots of p95 CLW (top row) and p95 PCT_{19} (bottom row) compared with mean values of the HSRL2 parameter listed in the title and y-axis of each plot within environmental bins stratified using the AVAPS parameter listed in the title of the corresponding plot. AVAPS threshold values were from Test 2 (Table 2). In all plots, blue triangles, green circles, and black squares correspond to data points associated with low, medium, and high magnitudes, respectively, of the associated AVAPS parameter. Please note that the ranges of the x- and y-axes are not constant among the scatterplots shown.

Moving on to Fig. 3b, a similar trend as Fig. 3a can be seen, where there is a considerable clustering of datapoints around CLW = 0 kg m^{-2}, including for several of the highest Bsc_{532} values (i.e., > 2 Mm^{-1} sr^{-1}). This further raises the question of cloud-free versus cloud-masked scenes, which will be explored more in this section and the next. It was interesting to see that the highest CLW values (e.g., > 0.5 kg m^{-2}) were associated with some of the lowest aerosol

concentrations and low-to-medium $LR_{850\text{-}700}$ values, both of which are the opposite of our hypotheses. As noted previously, the lack of precipitation in the QC'd AMPR data likely contributed to these unexpected trends. The statistical significance of the high $LR_{850\text{-}700}$ group seems to have been impacted by the data points with $Bsc_{532} < 1$ Mm^{-1} sr^{-1} and AMPR CLW between 0.25–0.75 kg m^{-2}. Because of these data clusters and masking, it is difficult to discern some of the convective-aerosol correlations in Fig. 3b, but it is apparent that, within the precipitation-masked AMPR data, aerosol concentration is not directly correlated with the convective metric. However, the statistical significance is worthy of additional examination as part of future work.

To look into regions where AMPR's CLW retrievals were masked in and around precipitation, AMPR T_b values can be used to obtain PCTs in these regions. Correlation coefficients between AMPR's 19.35-GHz PCT and the HSRL2 parameters are shown in Fig. 4. For brevity, only PCT_{19} is detailed herein given its sensitivity to clouds and precipitation, with additional PCT results presented in supplemental material. From Fig. 4 the correlation coefficient magnitudes were considerably lower than the AMPR CLW analysis but some positive correlations were present, including ones with statistical significance. This illustrates the benefits of examining PCT in regions of precipitation as opposed to solely relying on the CLW retrievals. To examine some of the correlations with greatest positive statistical significance in more detail, we have produced scatterplots of PCT_{19} versus Bsc_{355} when binned by LCL (Fig. 3c) and PCT_{19} versus Bsc_{355} when binned by $LR_{850\text{-}500}$ (Fig. 3d).

When examining the PCT_{19} values in Fig. 3c, many data points are are < 200 K, which indicates a relative lack of considerable precipitation in those scenes (Amiot et al., 2021; Amiot 2023); however, several data points with PCT_{19} > 200 K can be seen in Fig. 3c, including values > 260 K, which indicates that PCT_{19} is indeed capturing precipitation. There is considerable clustering of the data between a PCT_{19} of 185–200 K and Bsc_{355} of 0–7.5 Mm^{-1} sr^{-1}, suggesting the presence of several instances of clouds that were generally not precipitating. The association of the highest PCT_{19} values with relatively low aerosol concentrations (i.e., < 4 Mm^{-1} sr^{-1} in this case) within the low and medium LCL groups, combined with the clustering of data points mentioned previously, seems to have caused the extremely low correlation values for these low and medium groups. It appears that the high LCL correlation was sensitive to the three outlier values with $PCT_{19} > 220$ K and $Bsc_{355} > 5$ Mm^{-1} sr^{-1}, which contributed to its high value; however, the fact that this correlation was found to have statistical significance indicates that it is worthy of further examination. In general, increased aerosol concentration was not strongly associated with enhanced convection in Fig. 3c. However, it is noteworthy that over half of the data points with $PCT_{19} > 240$ K were associated with a low LCL; this would indicate a relatively high amount of low-level water vapor content, wherein warm-phase convective invigoration may take place (e.g., Grabowski and Morrison, 2020); however, there are only nine data points with $PCT_{19} > 240$ K and the aerosol concentrations are relatively low, so this potential connection needs further analysis.

The impact of a reduced dataset size can be seen to an even greater degree in Fig. 3d, which contains far fewer data points compared to Fig. 3c due to $LR_{850\text{-}500}$ requiring data from the 500-hPa level. Despite this, a statistically significant positive correlation was found between the aerosol and convective metrics, but it was unexpected that this

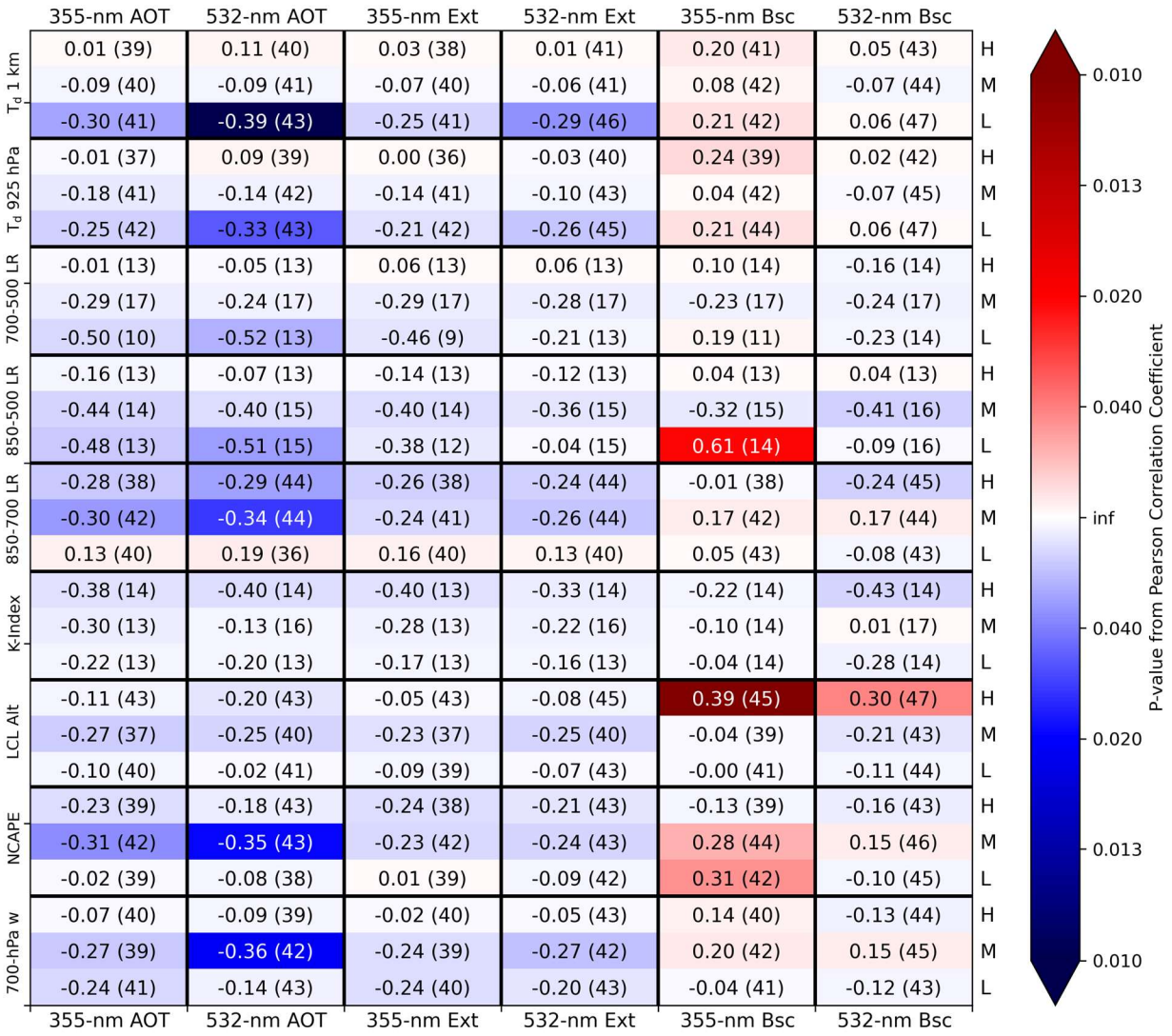

Figure 4: As in Fig. 2 but using p95 AMPR 19.35-GHz PCT as the convective parameter.

occurred for the low $LR_{850\text{-}500}$ group and not the medium or high groups. From Table 2, the low $LR_{850\text{-}500}$ values were still conditionally unstable and thus supportive of convection, so this result is physically plausible and deserved further analysis. However, it does seem that the data points with $PCT_{19} > 230$ K greatly influenced the correlations for the low and medium groups, which is to be expected with a relatively limited sample size. The increase in PCT_{19} with increasing aerosol concentration (within the low group) matches the hypothesized correlations, but the highest aerosol concentrations in Fig. 3d (i.e., $Bsc_{355} > 2$ Mm^{-1} sr^{-1} in this case) were associated with relatively low PCT_{19} values < 205 K in all but one instance. Thus, the overall trends in correlation between aerosol concentration and PCT_{19} in Fig. 3d are fairly mixed. Due to the presence of several statistically significant and potentially impactful results in Figs. 2, 3, and 4, future work should examine these and other AMPR data in greater detail. Lastly, as is true for all analyses in this study, while high correlation between two parameters is interesting and potentially significant, it does not guarantee a cause-and-effect situation between the parameters. Thus, the most noteworthy trends identified in this

428 study (e.g., Fig. 3) should be examined further to evaluate their significance and potential aerosol influences on convection. Many of these trends were also fairly consistent across the sensitivity tests (supplemental material).

430 **4. APR-3 results**

Similar analyses are presented in this section using $Z_{95,Ku}$. $Pixels_{Ku}$, and DFR as the convective parameters. All figures 432 utilize the AVAPS thresholds from Test 2 (Table 2), with the full sensitivity-test results presented in supplemental material. To begin, Pearson correlation coefficients between $Z_{95,Ku}$ and the HSRL2 variables can be seen in Fig. 5. 434 From Fig. 5, there is no widespread presence of statistically significant negative correlation coefficients was previously observed for the AMPR CLW, which further suggests that the precipitation flagging in AMPR CLW may explain the 436 negative correlations observed therein to some degree. On the contrary, several statistically significant positive correlations can be seen between $Z_{95,Ku}$ and the HSRL2 variables in Fig. 5. This is most notable when binning these 438 correlation analyses according to $NCAPE_{mod}$, LCL, lapse rate, and low-level T_d. While some correlations between $Z_{95,Ku}$ and the HSRL2 variables were relatively high (i.e., > 0.5) for the medium and high categories of some 440 environmental parameters (e.g., $LR_{850\text{-}500}$), it is interesting that the correlations within highest statistical significance were often associated with the low category of the environmental group. To examine some of these trends in greater 442 detail, the two parameters selected for more in-depth analysis from Fig. 5 were: 1) Bsc_{532} binned by LCL (Fig. 6a), and 2) Bsc_{355} binned by $NCAPE_{mod}$ (Fig. 6b); the former was selected based on its high statistical significance, while 444 the latter was selected to investigate the interesting negative correlations for medium $NCAPE_{mod}$.

In Fig. 6a, many $Z_{95,Ku}$ values > 30 dBZ were present in the CAMP^{2}Ex scenes, indicating that precipitating systems 446 were indeed flown over by the P-3 aircraft and further suggesting that AMPR's precipitation flags yielded many of the unexpected negative results in section 3. The standout feature of Fig. 6a is the statistically significant positive 448 correlation between $Z_{95,Ku}$ and Bsc_{532} when binned by low LCL values. That is, as aerosol concentration increased within low-LCL conditions, the peak Z_H within the same scene increased as well, suggesting the development of larger 450 raindrops. These large raindrops would dominate Z_H, but this analysis also highlights the importance of considering environmental conditions. This trend also supports the notion that, within low LCL group, which would have higher 452 lower-level water vapor content (all else being equal), higher $Z_{95,Ku}$ was associated with higher Bsc_{532} values. While this is limited by the relatively small sample size herein, this result matches the warm-phase invigoration of convection 454 discussed in prior studies (e.g., Grabowski and Morrison, 2020), and warrants further analysis. The correlation was also positive for the medium LCL group but with a lower correlation value and lesser statistical significance, indicating 456 the trend was not as robust as the low LCL group. Despite this, the trends of increasing $Z_{95,Ku}$ with increasing aerosol concentration in these groups matches physical expectations. It is also noteworthy that these trends were constant 458 across the sensitivity tests, increasing the reliability of these results. However, the negative correlation in the high LCL group was unexpected and seems to have been influenced by the upper-left data points in Fig. 6a.

460 Comparing $Z_{95,Ku}$ with Bsc_{355} when binned by $NCAPE_{mod}$ (Fig. 6b), positive correlations between $Z_{95,Ku}$ and Bsc_{355} were present for the low and high $NCAPE_{mod}$ groups, which matches expectations. However, the negative correlation

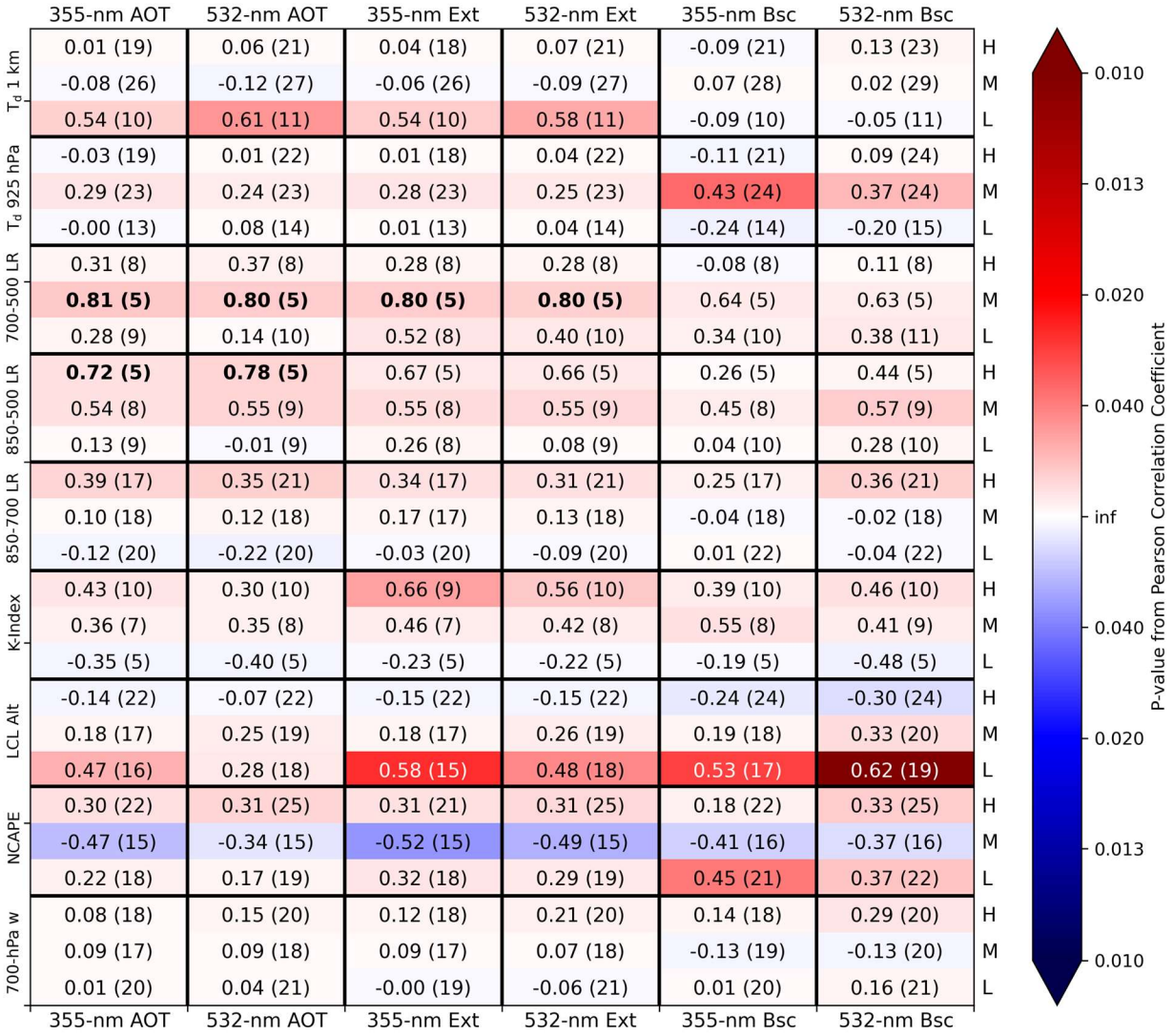

	355-nm AOT	532-nm AOT	355-nm Ext	532-nm Ext	355-nm Bsc	532-nm Bsc	
T_d 1 km	0.01 (19)	0.06 (21)	0.04 (18)	0.07 (21)	-0.09 (21)	0.13 (23)	H
	-0.08 (26)	-0.12 (27)	-0.06 (26)	-0.09 (27)	0.07 (28)	0.02 (29)	M
	0.54 (10)	0.61 (11)	0.54 (10)	0.58 (11)	-0.09 (10)	-0.05 (11)	L
T_d 925 hPa	-0.03 (19)	0.01 (22)	0.01 (18)	0.04 (22)	-0.11 (21)	0.09 (24)	H
	0.29 (23)	0.24 (23)	0.28 (23)	0.25 (23)	0.43 (24)	0.37 (24)	M
	-0.00 (13)	0.08 (14)	0.01 (13)	0.04 (14)	-0.24 (14)	-0.20 (15)	L
700-500 LR	0.31 (8)	0.37 (8)	0.28 (8)	0.28 (8)	-0.08 (8)	0.11 (8)	H
	0.81 (5)	**0.80 (5)**	**0.80 (5)**	**0.80 (5)**	0.64 (5)	0.63 (5)	M
	0.28 (9)	0.14 (10)	0.52 (8)	0.40 (10)	0.34 (10)	0.38 (11)	L
850-500 LR	**0.72 (5)**	**0.78 (5)**	0.67 (5)	0.66 (5)	0.26 (5)	0.44 (5)	H
	0.54 (8)	0.55 (9)	0.55 (8)	0.55 (9)	0.45 (8)	0.57 (9)	M
	0.13 (9)	-0.01 (9)	0.26 (8)	0.08 (9)	0.04 (10)	0.28 (10)	L
850-700 LR	0.39 (17)	0.35 (21)	0.34 (17)	0.31 (21)	0.25 (17)	0.36 (21)	H
	0.10 (18)	0.12 (18)	0.17 (17)	0.13 (18)	-0.04 (18)	-0.02 (18)	M
	-0.12 (20)	-0.22 (20)	-0.03 (20)	-0.09 (20)	0.01 (22)	-0.04 (22)	L
K-Index	0.43 (10)	0.30 (10)	0.66 (9)	0.56 (10)	0.39 (10)	0.46 (10)	H
	0.36 (7)	0.35 (8)	0.46 (7)	0.42 (8)	0.55 (8)	0.41 (9)	M
	-0.35 (5)	-0.40 (5)	-0.23 (5)	-0.22 (5)	-0.19 (5)	-0.48 (5)	L
LCL Alt	-0.14 (22)	-0.07 (22)	-0.15 (22)	-0.15 (22)	-0.24 (24)	-0.30 (24)	H
	0.18 (17)	0.25 (19)	0.18 (17)	0.26 (19)	0.19 (18)	0.33 (20)	M
	0.47 (16)	0.28 (18)	0.58 (15)	0.48 (18)	0.53 (17)	0.62 (19)	L
NCAPE	0.30 (22)	0.31 (25)	0.31 (21)	0.31 (25)	0.18 (22)	0.33 (25)	H
	-0.47 (15)	-0.34 (15)	-0.52 (15)	-0.49 (15)	-0.41 (16)	-0.37 (16)	M
	0.22 (18)	0.17 (19)	0.32 (18)	0.29 (19)	0.45 (21)	0.37 (22)	L
700-hPa w	0.08 (18)	0.15 (20)	0.12 (18)	0.21 (20)	0.14 (18)	0.29 (20)	H
	0.09 (17)	0.09 (18)	0.09 (17)	0.07 (18)	-0.13 (19)	-0.13 (20)	M
	0.01 (20)	0.04 (21)	-0.00 (19)	-0.06 (21)	0.01 (20)	0.16 (21)	L
	355-nm AOT	532-nm AOT	355-nm Ext	532-nm Ext	355-nm Bsc	532-nm Bsc	

Figure 5: As in Fig. 2 but using p95 APR-3 Ku-band composite Z_H as the convective parameter.

within the medium $NCAPE_{mod}$ group was unexpected – this appears to be the result of only two data points with $Z_{95,Ku}$ > 40 dBZ in this medium group, unlike the low and high groups, which suggests that the medium $NCAPE_{mod}$ values were not as supportive of convection. The presence of Bsc_{355} > 4 Mm^{-1} sr^{-1} associated with $Z_{95,Ku}$ > 50 dBZ within the high $NCAPE_{mod}$ is interesting as it suggests that the aerosol conditions may have supported the development of deeper convection when environmental conditions were more suitable for convection in general; however, this trend was not constant, as the highest $Z_{95,Ku}$ values were associated with Bsc_{355} < 4 Mm^{-1} sr^{-1} and low $NCAPE_{mod}$ values, which indicates that this analysis warrants further examination. It should also be stressed that the presence of high correlations do not guarantee causality, further indicating that these results should be examined further.

Next, the number of APR-3 Ku-band composite Z_H pixels ≥ 30 dBZ (i.e., $Pixels_{Ku}$) was used as the convective parameter (Fig. 7). Several more highly positive correlations were present compared to Figs. 2, 4, and 5, likely due

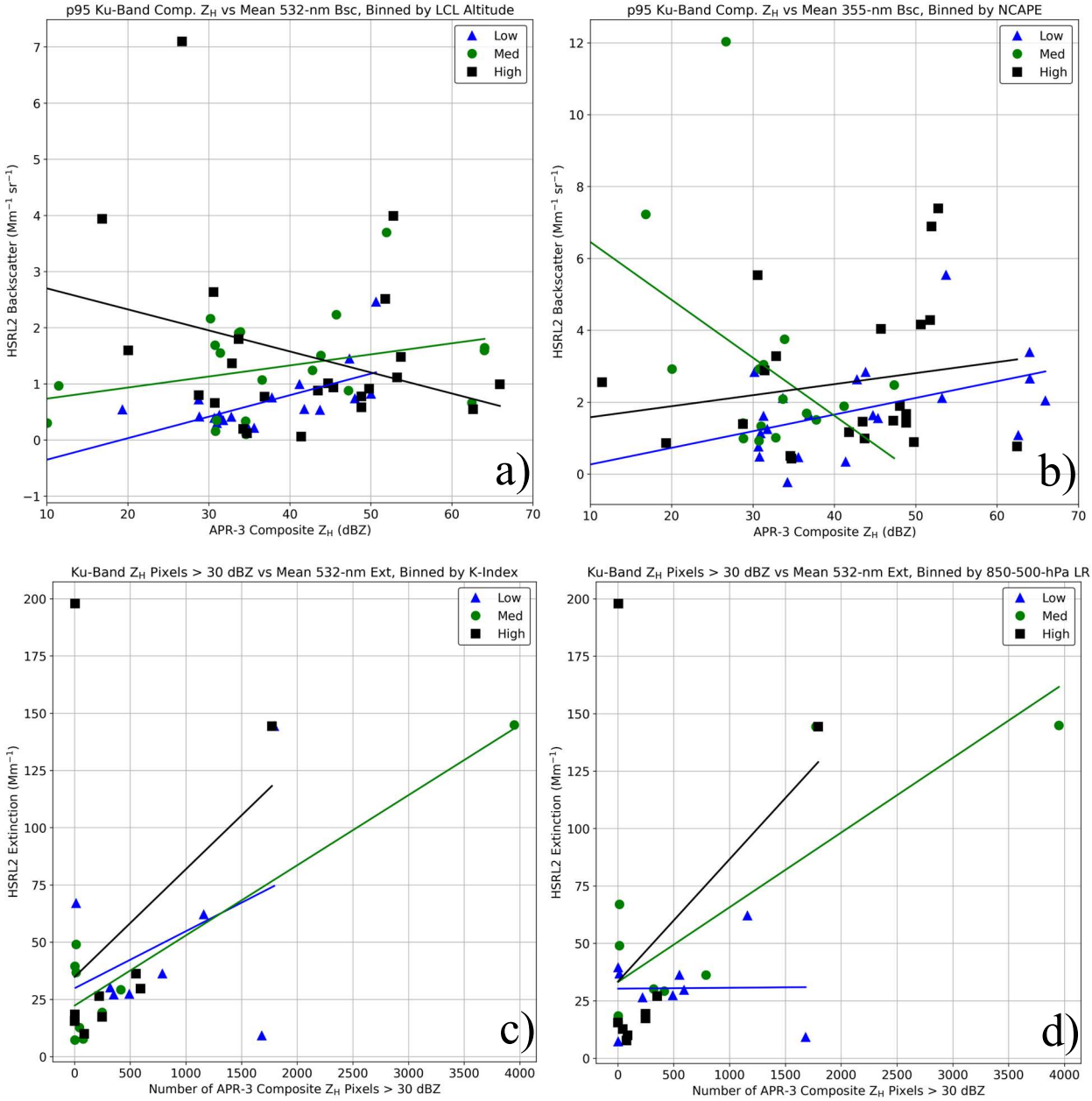

Figure 6: As in Fig. 3, but these are scatterplots of p95 APR-3 Ku-band composite Z_H (top row) and the number of APR-3 Ku-band composite Z_H pixels ≥ 30 dBZ (bottom row) compared against the mean value of the HSRL2 parameter listed in the title of each plot. The AVAPS parameter used to stratify the environments is also listed in the title of each plot.

to $Pixels_{Ku}$ focusing on the abundance of convection rather than a peak value in a given scene. The strongest positive correlations with a statistically significant p-value were found between $Pixels_{Ku}$ and lapse rate, K-Index, and LCL. Given their statistical significance, the decision was made to examine the strong correlations between $Pixels_{Ku}$ and Ext_{532} within environments binned by K-Index (Fig. 6c) and $LR_{850\text{-}500}$ (Fig. 6d). From Fig. 6c, most scenes featured at least one Ku-band composite Z_H observation > 30 dBZ, further indicating the precipitating clouds the P-3 passed

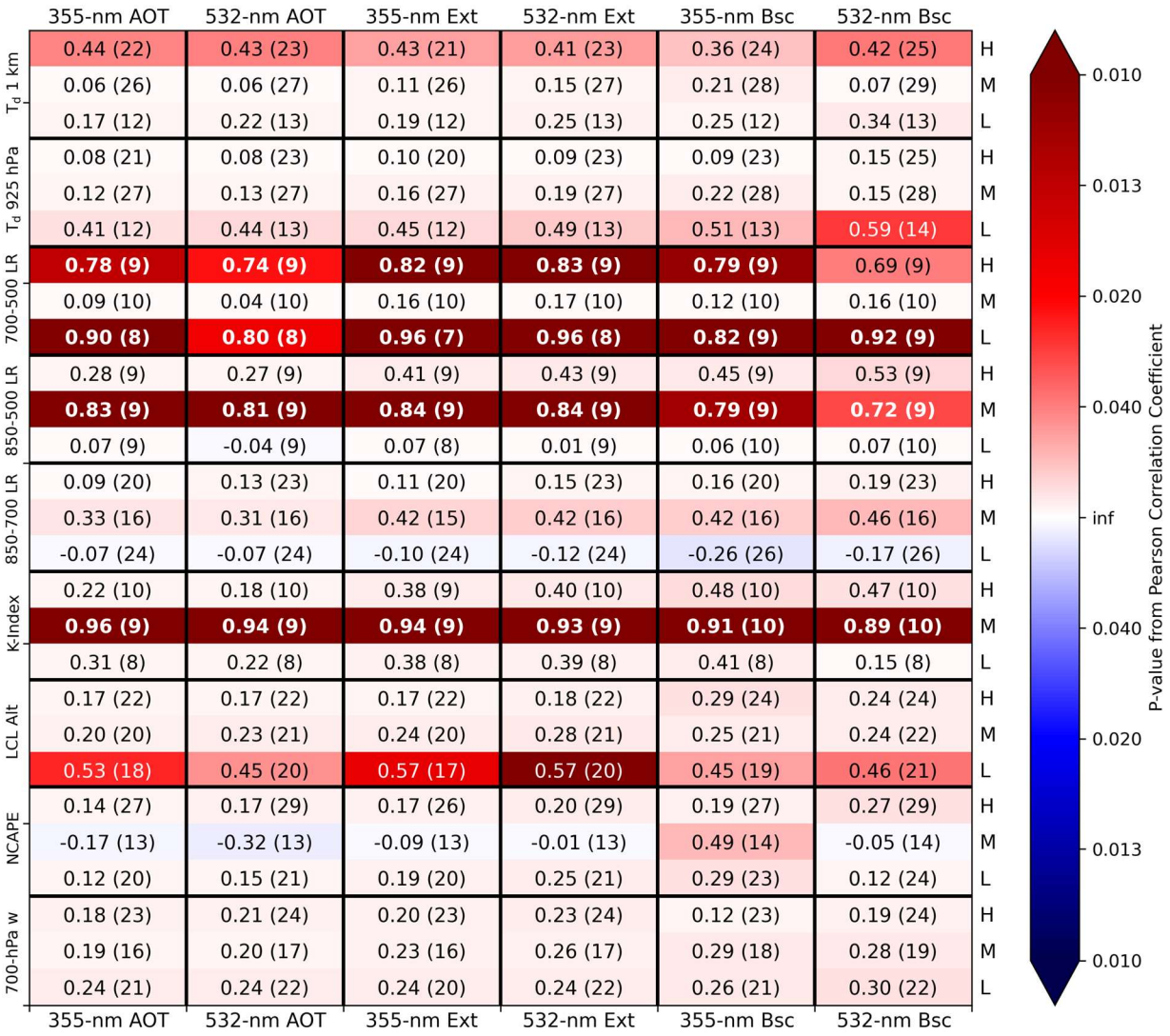

482 **Figure 7: As in Fig. 2 but using the number of APR-3 Ku-band composite Z_H pixels ≥ 30 dBZ as the convective parameter.**

484 over during CAMP^{2}Ex. In Fig. 6c, with the available data, the general trend was an increase in $Pixels_{Ku}$ with increasing Ext_{532} for all categories of K-Index. The general trend matches expectations that higher aerosol concentrations would
486 be correlated with a general abundance of convection and the formation of fewer but larger raindrops in a given scene. Further, it seems that higher aerosol concentrations supported the development of convection in general within a given
488 scene, regardless of whether these APR-3 pixels were part of a single large convective storm or several individual plume However, it was also anticipated that the highest $Pixels_{Ku}$ would be associated with the highest K-Index values,
490 which is generally not the case. This may be explained by the considerably small sample size in Fig. 6c, which limits the statistical significance of results obtained from Fig. 6c. The impact of the small sample size also causes the best-
492 fit lines to be impacted by some of the outlier values, such as the data points in the medium and high K-Index group with $Pixels_{Ku} > 1500$.

Similar trends can be found when comparing $Pixels_{Ku}$ with Ext_{532} in environments binned by $LR_{850\text{-}500}$, particularly for the medium and high groups (Fig. 6d). That is, increased aerosol concentration was generally correlated with increased $Pixels_{Ku}$ for each of the environmental bins, suggesting the potential for the higher aerosol concentrations to yield larger raindrops throughout the scene. However, the correlation was only statistically significant for the medium group and was nearly zero for the low group. These results further indicate the impact of the small sample size on this comparison, but the statistical significance of the correlations for the medium group of $LR_{850\text{-}500}$ warrant further examination. As with the prior analyses, it must also be noted that correlation does not guarantee causation, and thus the statistically significant results would benefit from expanded analyses using a larger sample size.

Lastly, DFR was used as the convective metric (Fig. 8). As with $Z_{95,Ku}$ and unlike $Pixels_{Ku}$, DFR focuses on the intensity of a given convective storm rather than the overall abundance of convection. From Fig. 8, the most statistically significant and strongest correlations were found when binning the environments according to $NCAPE_{mod}$ and $LR_{850\text{-}700}$ but, unexpectedly, were typically in association with low values of these environmental conditions. Due to the presence of several statistically significant correlations, these two environmental parameters were selected for a more in-depth analysis. In particular, DFR was compared with Bsc_{532} when binned by $LR_{850\text{-}700}$ (Fig. 9a) and $NCAPE_{mod}$ (Fig. 9b). Examining Fig. 9a, all three environmental groups were associated with positive correlations between DFR and Bsc_{532}, though these two parameters had essentially no correlation in the medium aerosol group. The strongest and most statistically significant correlation was in association with the low $LR_{850\text{-}700}$ group; this was unexpected but, as seen in Table 2, these lapse rate values were still conditionally unstable and supportive of convection in the maritime tropics. The trend of increasing DFR with increasing aerosol concentration matches expectations that, as raindrops grow, the Ka-band APR-3 signal would become more attenuated and yield a higher DFR. It is also noteworthy that the highest DFR values > 30 dBZ (albeit a relatively limited sample size) were associated with relatively "medium" aerosol concentrations (i.e., Bsc_{532} of approximately 1.0–2.5 Mm^{-1} sr^{-1}). This matches the "Goldilocks" zone of medium aerosol concentration favoring enhanced convection (e.g., Sokolowsky et al., 2022). Given the potential presence of these "Goldilocks" conditions and the statistical significance within the low group in Fig. 9a, these trends warrant further investigation.

Some similar trends can be seen in Fig. 9b, where binning the environment by $NCAPE_{mod}$ yielded statistically significant correlations between DFR and Bsc_{532} within low $NCAPE_{mod}$ scenes. This statistical significance occurring in the low $NCAPE_{mod}$ group was unexpected but, as seen in Table 2, these $NCAPE_{mod}$ values were still associated with upward acceleration (i.e., conditions favoring enhanced convection). For each $NCAPE_{mod}$ group, higher aerosol concentrations were generally correlated with higher DFR values, suggesting conditions wherein raindrops may have grown large enough to significantly attenuate the Ka-band APR-3 signal. The "Goldilocks" zone of medium aerosol concentration with Bsc_{532} of approximately 1.0–2.5 Mm^{-1} sr^{-1} is present in Fig. 9b as well, indicating its persistence across different environmental binning techniques. Many of the DFR trends, including those examined in Fig. 9, were

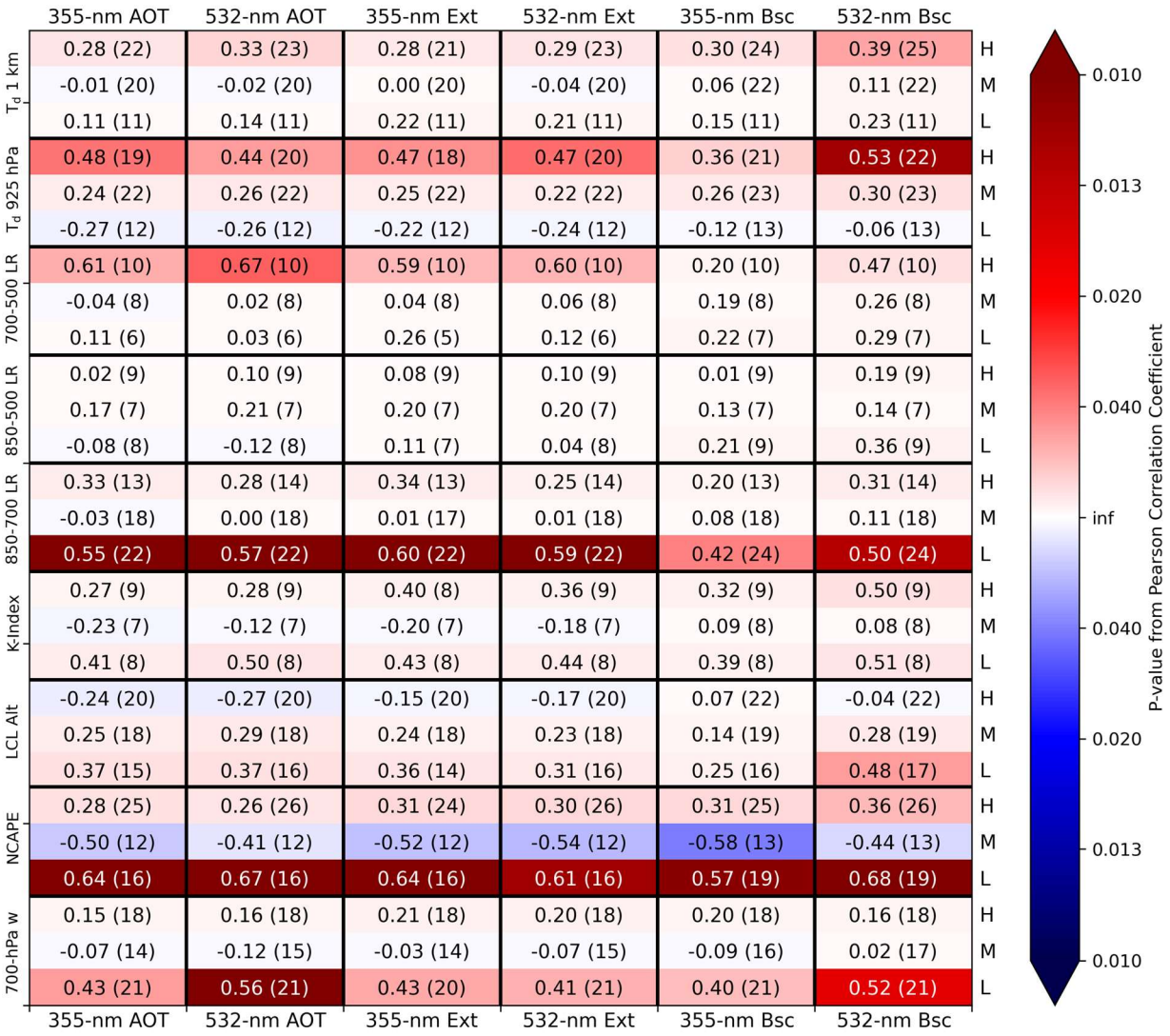

Figure 8: As in Fig. 2 but using p95 Ku-/Ka-band DFR as the convective parameter.

relatively consistent across the sensitivity tests (supplemental material), but other trends varied across the sensitivity tests and suggests that several of data points may have fallen at the edges of the values used to bin the environments.

5. Summary, limitations, and future work

This study focused on examining potential impacts of aerosol concentration on maritime tropical convection using remote-sensing data in environmental contexts. Nine parameters from 92 AVAPS dropsondes across CAMP^{2}Ex SFs 05–19 were used to stratify the environments: 700-hPa vertical velocity; modified CAPE; LCL altitude; K-Index; 850–700-, 850–500-, and 700–500-hPa temperature lapse rates; mean T_d below 1 km AGL; and mean T_d below 925 hPa. Each dropsonde launch time was associated with a corresponding APR-3 scan, whose file start and end times

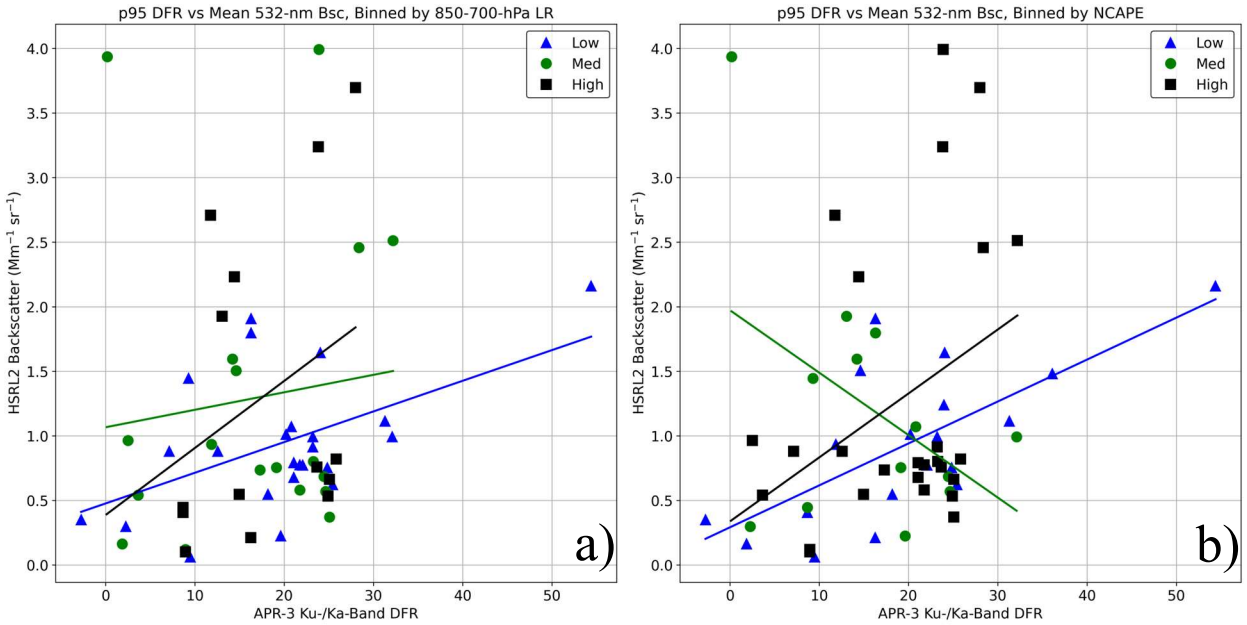

536 **Figure 9: As in Fig. 3, but these are scatterplots of p95 APR-3 Ku-/Ka-band DFR compared against the mean**
537 **value of the HSRL2 parameter listed in the title of each plot. The AVAPS parameter used to stratify the**
538 **environments is also listed in the title of each plot.**

were used to develop a 10-minute "scene" for all comparisons associated with the given dropsonde. Threshold values
540 were selected to divide scenes into "low," "medium," and "high" groups based on each AVAPS parameter, and sensitivity testing examined four different sets of threshold values used for each stratification. Eight AMPR and APR-
542 3 metrics related to convective intensity and/or prevalence were compared with HSRL2 backscatter, extinction, and AOT at 355 and 532 nm within the binned environments using Pearson correlation coefficients and their associated
544 p-values. These convective parameters were: p95 of AMPR CLW; p95 of PCT at 10.7, 19.35, 37.1, and 85.5 GHz; p95 of APR-3 Ku-band composite Z_H; number of Ku-band composite Z_H pixels ≥ 30 dBZ; and Ku-/Ka-band DFR.

546 The correlations between the convective metrics and aerosol parameters varied depending on which convective metric was examined. Largely because of masking regions of precipitation in its analysis, AMPR CLW and PCT_{19} were
548 often unexpectedly negatively correlated with aerosol concentration within each environmental group examined, including to a statistically significant degree in many cases. The masking of precipitation regions in AMPR's CLW
550 analyses yielded several unexpected negative correlations and limited the aerosol-convection conclusions that could be drawn solely based on AMPR CLW. This was mitigated when examining AMPR PCT_{19}, which includes
552 precipitation regions and yielded several positive aerosol-convection correlations as expected, some of which had statistical significance. Likewise, examining APR-3's $Z_{95,Ku}$, $Pixels_{Ku}$, and DFR yielded many positive correlations
554 with aerosol concentration, including several with statistical significance. While $Pixels_{Ku}$ was limited by a fairly small sample size in some cases, a trend of increasing $Pixels_{Ku}$ with increasing aerosol concentration could be seen in the
556 scatterplots. The main feature of the $Z_{95,Ku}$ analysis was its relatively strong and statistically significant correlation with aerosol concentrations in environments with a low LCL, indicating a relatively high amount of low-level water

vapor and supporting the idea raised in past studies that increased aerosol concentration may enhance convection within warm-phase regions. A standout result of the DFR analysis was the presence of a "Goldilocks" zone of medium aerosol concentration, suggesting that these medium values enhanced convection to a stronger degree than low or high aerosol concentrations in some cases, as also observed in prior studies. Correlations between aerosol concentrations and the convective parameters occasionally became more highly positive and more statistically significant, based on the associated p-value, as environmental conditions became more favorable for convection overall, which matches our hypotheses.

These results are important as they highlight some potentially impactful correlations between convective parameters and aerosol concentrations in the maritime tropics, including some instances where medium-to-high aerosol concentrations appeared supportive of convective invigoration. However, as noted throughout the manuscript, correlation does not necessarily indicate causation. Because of this, correlations highlighted in this study serve to identify potentially interesting and impactful trends that warrant a more in-depth exploration in future work, rather than providing solid definitive conclusions on their own. Our results also stress the importance of considering environmental conditions alongside aerosol concentrations when evaluating impacts on convection. Further, the correlation tables presented in this manuscript, including those in supplemental material, provide a wide range of information that is applicable to broader applications (e.g., a future study that might explore the impacts of low-level Td or mid-level lapse rates on tropical convection).

While many results were encouraging, several limitations must be considered. Dropsondes launched when the P-3 was above 500 hPa were relatively limited, reducing the sample size for all associated environmental parameters. Other limitations in the dataset, such as the P-3 avoiding the most intense convection during a given flight and environmental modification from nearby convection, impacted the results. There was some ambiguity regarding whether an increase in $\text{Pixels}_{\text{Ku}}$ was associated with a single updraft or multiple updrafts, which have different implications for convective intensity and prevalence. Lastly, while many correlations were strong and encouraging, they do not necessarily prove a cause-and-effect situation for their respective comparison, as previously discussed. Thus, it is not possible to say with certainty that increased aerosol concentrations enhanced convection in these CAMP^{2}Ex scenes solely based on the correlations presented in this study, but rather the data suggest the possibility for aerosol enhancement of convection and further analyses would increase confidence in these results.

Given the encouraging nature of many comparisons in this study, while also considering the above limitations, future work would greatly benefit these science questions. Future efforts could look at addressing the limitations above, such as using an advanced Z_H attenuation-correction method, distinguishing areas where $\text{Pixels}_{\text{Ku}}$ were adjacent or separated, and employing other datasets from the P-3 and Learjet-35 aircraft to increase reliability of the strongest correlations observed. Peak 30-dBZ Z_H contour height in a storm should be considered given its direct relation to updraft magnitude (e.g., Straka et al., 2000; Amiot et al., 2019). Other remote-sensing data (e.g., satellite) may help with assessing nearby convection just outside of the P-3 observation range. Additional environmental parameters,

such as wet-bulb potential temperature profiles (Williams and Renno, 1993), would be useful to examine. Other aerosol properties (e.g., type, composition, and hygroscopicity) and their vertical location/distribution may also be helpful to consider. Examining some of the most-significant convective-aerosol correlations in greater detail would also be of significant benefit, as would separating the scenes according to the type of convection observed (e.g., shallow versus congestus).

Data availability

The AMPR, APR-3, AVAPS, and HSRL2 data are available on the NASA Langley Research Center's Airborne Science Data for Atmospheric Composition repository at https://www-air.larc.nasa.gov/cgi-bin/ArcView/camp2ex, cited herein as Aknan and Chen (2020). The objective selections of threshold values for environmental stratification were performed using Python's NumPy nanpercentile function (Harris et al., 2020). Pearson correlation coefficients and p-values were calculated using Python's SciPy pearsonr function (Virtanen et al., 2020). Several of the environmental parameters were calculated using Python's MetPy package (May et al., 2022), including the mixed_layer_cape_cin function for $CAPE_{mod}$, the calc.lcl function for LCL altitude, and SkewT function for producing the dropsonde image in Fig. 1.

Author contributions

CGA performed all primary analyses and wrote the manuscript with feedback and contributions from all co-authors. TJL supervised the study, served as AMPR Principal Investigator (PI), and assisted with refining the methods and interpreting results. CGA and TJL processed the AMPR data. SCvdH and RAF served as PI for AVAPS and HSRL2, respectively. OOS processed the APR-3 data. SCvdH, RAF, OOS, LDC, SAC, and JRM assisted with refining the methods and interpreting results. SWF and GAS processed the AVAPS data. CAH processed the HSRL2 data. ST served as APR-3 PI.

Competing interests

The authors declare that they have no conflict of interest.

Acknowledgements

We are grateful to Hal Maring for financial support throughout the CAMP^{2}Ex deployment and data analyses, and to Jeff Reid for managing the CAMP^{2}Ex mission. We would also like to thank Wojciech Grabowski and one anonymous reviewer for their insightful comments and suggestions that helped improve this manuscript.

Financial support

CGA acknowledges funding from NASA Marshall Space Flight Center through Cooperative Agreement 80MSFC22M0001 with The University of Alabama in Huntsville. CGA's research was further supported by an

appointment to the NASA Postdoctoral Program at NASA Marshall Space Flight Center, administered by Oak Ridge Associated Universities under contract with NASA, through contract 80HQTR21CA005.

References

Aknan, A., and Chen, G.: Joint data repository – CAMP2Ex, PISTON, NASA Langley Research Center, https://www-air.larc.nasa.gov/missions/camp2ex/index.html, accessed: 16 November 2020.

Albrecht, B. A.: Aerosols, cloud microphysics, and fractional cloudiness. Science, 245, 1227–1230, https://doi.org/10.1126/science.245.4923.1227, 1989.

Altaratz, O., Koren, I., Resin, Y., Kostinski, A., Feingold, G., Levin, Z., and Yin, Y.: Aerosols' influence on the interplay between condensation, evaporation and rain in warm cumulus cloud. Atmos. Chem. Phys., 8, 15–24, https://doi.org/10.5194/acp-8-15-2008, 2008.

Amiot, C. G.: Airborne passive microwave geophysical retrievals and applications in assessing environmental and aerosol impacts on maritime convection. Ph.D. dissertation, Dept. of Atmospheric and Earth Science, The University of Alabama in Huntsville, Huntsville, AL, 176 pp, https://louis.uah.edu/uah-dissertations/278/, 2023.

Amiot, C. G., Carey, L. D., Roeder, W. P., McNamara, T. M., and Blakeslee, R. J.: C-band dual-polarization radar signatures of wet downbursts around Cape Canaveral, Florida. Weather Forecast., 34, 103–131, https://doi.org/10.1175/WAF-D-18-0081.1, 2019.

Amiot, C. G., Biswas, S. K., Lang, T. J., and Duncan, D. I.: Dual-polarization deconvolution and geophysical retrievals from the Advanced Microwave Precipitation Radiometer during OLYMPEX/RADEX. J. Atmos. Ocean. Tech., 38, 607–628, https://doi.org/10.1175/JTECH-D-19-0218.1, 2021.

Atmosphere Observing System (AOS): Atmosphere Observing System, National Aeronautics and Space Administration, https://aos.gsfc.nasa.gov/, accessed: 16 March 2022.

Bhargava, K., Kalnay, E., Carton, J. A., and Yang, F.: Estimation of systematic errors in the GFS using analysis increments. J. Geophys. Res.-Atmos., 123, 1626–1637, https://doi.org/10.1002/2017JD027423, 2018.

Blanchard, D. O.: Assessing the vertical distribution of convective available potential energy. Weather Forecast., 13, 870–877, https://doi.org/10.1175/1520-0434(1998)013<0870:ATVDOC>2.0.CO;2, 1998.

Bony, S., Dufresne, J. L., Le Treut, H., Morcrette, J. J., and Senior, C.: On dynamic and thermodynamic components of cloud changes. *Clim. Dynam.*, **22**, 71–86, https://doi.org/10.1007/s00382-003-0369-6, 2004.

Burton, S. P., and Coauthors: Observations of the spectral dependence of linear particle depolarization ratio of aerosols using NASA Langley airborne High Spectral Resolution Lidar. Atmos. Chem. Phys., 15, 13453–13473, https://doi.org/10.5194/acp-15-13453-2015, 2015.

Burton, S. P., and Coauthors: Information content and sensitivity of the $3\beta + 2\alpha$ lidar measurement system for aerosol microphysical retrievals. Atmos. Meas. Tech., 9, 555 –5574, https://doi.org/10.5194/amt-9-5555-2016, 2016.

Burton, S. P., and Coauthors: Calibration of a high spectral resolution lidar using a Michelson interferometer with data examples from ORACLES. Appl. Optics, 57, 6061–6075, https://doi.org/10.1364/AO.57.006061, 2018.

Cecil, D. J., and Chronis, T.: Polarization-corrected temperatures for 10-, 19-, 37-, and 89-GHz passive microwave frequencies. J. Appl. Meteorol. Clim., 57, 2249–2265, https://doi.org/10.1175/JAMC-D-18-0022.1, 2018.

Chand, D., Wood, R., Anderson, T. L., Satheesh, S. K., and Carlson, R. J.: Satellite-derived direct radiative effect of aerosols dependent on cloud cover. Nat. Geosci., 2, 181–184, https://doi.org/10.1038/ngeo437, 2009.

Cotton, W. R., and Walko, R.: Examination of aerosol-induced convective invigoration using idealized simulations. J. Atmos. Sci., 78, 287–298, https://doi.org/10.1175/JAS-D-20-0023.1, 2021.

Durden, S., Tanelli, S., and Sy, O. O.: Product handbook for the Airborne Precipitation Radar Third Generation (APR3, all products): CAMP2Ex version 2, NASA Langley Research Center, 15 pp, https://www-air.larc.nasa.gov/cgi-bin/ArcView/camp2ex, 2020.

Earth Science Project Office (ESPO): CAMP2Ex, NASA Ames Research Center, https://espo.nasa.gov/camp2ex/content/CAMP2Ex, accessed: 25 April 2020.

Fan, J., and Coauthors: Substantial convection and precipitation enhancements by ultrafine aerosol particles. Science, 359, 411 – 418, https://doi.org/10.1126/science.aan8461, 2018.

Ferrare, R., and Coauthors: Airborne HSRL-2 measurements of elevated aerosol depolarization associated with non-spherical sea salt. Front. Remote Sens., 4:1143944, https://doi.org/10.3389/frsen.2023.1143944, 2023.

Freeman, S., Sokolowsky, G. A., and van den Heever, S. C.: CAMP2Ex AVAPS readme/quick start guide, NASA Langley Research Center, 6 pp, https://www-air.larc.nasa.gov/cgi-bin/ArcView/camp2ex, 2020.

Fritz, J., and Chandrasekar, V.: Simulating radar observations of precipitation at higher frequencies from lower-frequency polarimetric measurements. J. Atmos. Ocean. Tech., 29, 1435–1454, https://doi.org/10.1175/JTECH-D-11-00157.1, 2012.

Grabowski, W. W.: Can the impact of aerosols on deep convection be isolated from meteorological effects in atmospheric observations?. J. Atmos. Sci., 75, 3347–3363, https://doi.org/10.1175/JAS-D-18-0105.1, 2018.

Grabowski, W. W.: Daytime convective development over land: The role of surface forcing. Q J Roy Meteor Soc, 149, 2800–2819, https://doi.org/10.1002/qj.4532, 2023.

Grabowski, W. W., and Morrison, H.: Untangling microphysical impacts on deep convection applying a novel modeling methodology. Part II: Double-moment microphysics. J. Atmos. Sci., 73, 3749–3770, https://doi.org/10.1175/JAS-D-15-0367.1, 2016.

Grabowski, W. W., and Morrison, H.: Modeling condensation in deep convection. J. Atmos. Sci., 74, 2247–2267, https://doi.org/10.1175/JAS-D-16-0255.1, 2017.

Grabowski, W. W. and Morrison, H.: Do Ultrafine Cloud Condensation Nuclei Invigorate Deep Convection?, J. Atmos. Sci., 77, 2567–2583, https://doi.org/10.1175/JAS-D-20-0012.1, 2020.

George, J. J.: *Weather Forecasting for Aeronautics*. Academic Press, 673 pp, ISBN 9781483256450, 1960.

Harris, C. R., and Coauthors: Array programming with NumPy. Nature, 585, 357–362, https://doi.org/10.1038/s41586-020-2649-2, 2020.

Hastings, R., and Richardson, R.: Long-term morphological changes in simulated supercells following mergers with nascent supercells in directionally varying shear. Mon. Weather Rev., 144, 471–499, https://doi.org/10.1175/MWR-D-15-0193, 2016.

Hock, T., and Young, K.: GPM Ground Validation Advanced Vertical Atmospheric Profiling System (AVAPS) OLYMPEX, NASA Global Hydrology Resource Center DAAC, http://dx.doi.org/10.5067/GPMGV/OLYMPEX/AVAPS/DATA101, accessed: 13 June 2019, 2017.

Hogan, R. J., Gaussiat, N., and Illingworth, A. I.: Stratocumulus liquid water content from dual-wavelength radar. J. Atmos. Ocean. Tech., 22, 1207–1218, https://doi.org/10.1175/JTECH1768.1, 2005.

Hong, S., and Shin, I.: Wind speed retrieval based on sea surface roughness measurements from spaceborne microwave radiometers. J. Appl. Meteorol. Clim., 52, 507–516, https://doi.org/10.1175/JAMC-D-11-0209.1, 2013.

Hostetler, C. A.: CAMP2Ex HSRL-2 ReadMe, NASA Langley Research Center, 1 pp, https://www-air.larc.nasa.gov/cgi-bin/ArcView/camp2ex, 2020.

Igel, A. L., and van den Heever, S. C.: Invigoration or enervation of convective clouds by aerosols? Geophys. Res. Lett., 48, e2021GL093804, https://doi.org/10.1029/2021GL093804, 2021.

Jiang, H., and Zipser, E. J.: Retrieval of hydrometeor profiles in tropical cyclones and convection from combined radar and radiometer observations. J. Appl. Meteorol. Clim., 45, 1096–1115, https://doi.org/10.1175/JAM2386.1, 2006.

Johnson, J. T., MacKeen, P. L., Witt, A., Mitchell, E. D., Stumpf, G. J., Eilts, M. D., and Thomas, K. W.: The Storm Cell Identification and Tracking Algorithm: An enhanced WSR-88D algorithm. Weather Forecast., 13, 263–276, https://doi.org/10.1175/1520-0434(1998)013<0263:TSCIAT>2.0.CO;2, 1998.

Junge, C., and McLaren, E.: Relationship of cloud nuclei spectra to aerosol size distribution and composition. J. Atmos. Sci., 28, 382–390, https://doi.org/10.1175/1520-0469(1971)028<0382:ROCNST>2.0.CO;2, 1971.

Kollias, P., Albrecht, B. A., Lhermitte, R., and Savtchenko, A.: Radar observations of updrafts, downdrafts, and turbulence in fair-weather cumuli. J. Atmos. Sci., 58, 1750–1766, https://doi.org/10.1175/1520-0469(2001)058<1750:ROOUDA>2.0.CO;2, 2001.

Kretschmer, M., Runge, J., and Coumou, D.: Early prediction of extreme stratospheric polar vortex states based on causal precursors. Geophys. Res. Lett., 44, 8592–8600, https://doi.org/10.1002/2017GL074696, 2017.

Lang, T., Amiot, C., and Biswas, S.: AMPR CAMP2Ex, calibrated & quality-controlled flight dataset, level 2B, revision 1, NASA Langley Research Center, 16 pp, https://www-air.larc.nasa.gov/cgi-bin/ArcView/camp2ex, 2021.

Lenhardt, E. D., and Coauthors: Use of lidar aerosol extinction and backscatter coefficients to estimate cloud condensation nuclei (CCN) concentrations in the southeast Atlantic. Atmos. Meas. Tech. [preprint], https://doi.org/10.5194/amt-2022-262, 2022.

Liao, L., and Meneghini, R.: A study on the feasibility of dual-wavelength radar for identification of hydrometeor phases. J. Appl. Meteorol. Clim., 50, 449–456, https://doi.org/10.1175/2010JAMC2499.1, 2011.

Liao, L., Meneghini, R., Tian, L., and Heymsfield, G. M.: Retrieval of snow and rain from combined X- and W-band airborne radar measurements. IEEE T. Geosci. Remote, 46, 1514–1524, https://doi.org/10.1109/TGRS.2008.916079, 2008.

Lin, J. C., Matsui, T., Pielke, R. A., and Kummerow, C.: Effects of biomass-burning-derived aerosols on precipitation and clouds in the Amazon Basin: a satellite-based empirical study. J. Geophys. Res.-Atmos., 111, D19204, https://doi.org/10.1029/2005JD006884, 2006.

Liu, J., Li, Z., and Cribb, M.: Response of marine boundary layer cloud properties to aerosol perturbations associated with meteorological conditions from the 19-month AMF-Azores campaign. J. Atmos. Sci., 73, 4253–4268, https://doi.org/10.1175/JAS-D-15-0364.1, 2016.

Lucas, C., Zipser, E. J., and Ferrier, B. S.: Sensitivity of tropical west Pacific oceanic squall lines to tropospheric wind and moisture profiles. J. Atmos. Sci., 57, 2351–2373, https://doi.org/10.1175/1520-0469(2000)057<2351:SOTWPO>2.0.CO;2, 2000.

Marinescu, P. J., and Coauthors: Impacts of varying concentrations of cloud condensation nuclei on deep convective cloud updrafts – A multimodel assessment. J. Atmos. Sci., 78, 1147–1172, https://doi.org/10.1175/JAS-D-20-0200.1, 2021.

Markowski, P., and Richardson, Y.: *Mesoscale Meteorology in Midlatitudes.* Wiley-Blackwell, 407 pp, ISBN 9781119966678, 2010.

May, R. M., and Coauthors: MetPy: A meteorological Python library for data analysis and visualization. B. Am. Meteorol. Soc., 103, E2273–E2284, https://doi.org/10.1175/BAMS-D-21-0125.1, 2022.

Mulholland, J. P., Peters, J. M., and Morrison, H.: How does LCL height influence deep convective updraft width?. Geophys. Res. Lett., 48, e2021GL093316, https://doi.org/10.1029/2021GL093316, 2021.

Orlanski, I.: A rational subdivision of scales for atmospheric processes. B. Am. Meteorol. Soc., 56, 527–530, https://doi.org/10.1175/1520-0477-56.5.527, 1975.

Redemann, J., and Coauthors: An overview of the ORACLES (ObseRvations of Aerosols above CLouds and their intEractionS) project: Aerosol-cloud-radiation interactions in the southeast Atlantic Basin. Atmos. Chem. Phys., 21, 1507 – 1563, https://doi.org/10.5194/acp-21-1507-2021, 2021.

Reid, J. S., and Coauthors: The coupling between tropical meteorology, aerosol lifecycle, convection and the energy budget: The Cloud, Aerosol and Monsoon Processes Philippines Experiment (CAMP2Ex). B. Am. Meteorol. Soc., 106, E1179–E1205, https://doi.org/10.1175/BAMS-D-21-0285.1, 2023.

Rinehart, R. E.: *Radar for Meteorologists*. Rinehart Publications, 482 pp, ISBN 9780965800211, 2010.

Rosenfeld, D., and Lensky, I. M.: Satellite-based insight into precipitation formation processes in continental and maritime convective clouds. B. Am. Meteorol. Soc., 79, 2457–2476, https://doi.org/10.1175/1520-0477(1998)079<2457:SBIIPF>2.0.CO;2, 1998.

Rosenfeld, D., Lohmann, U., Raga, G. B., O'Dowd, C. D., Kulmala, M., Fuzzi, S., Reissell, A., and Andreae, M. O.: Flood or drought: How do aerosols affect precipitation? Science, 321, 1309–1313, https://doi.org/10.1126/science.1160606, 2008.

Saleeby, S. M., Berg, W., van den Heever, S., and L'Ecuyer, T.: Impact of cloud-nucleating aerosols in cloud-resolving model simulations of warm-rain precipitation in the East China Sea. J. Atmos. Sci., 67, 3916–3930, https://doi.org/10.1175/2010JAS3528.1, 2010.

Sheffield, A. M., Saleeby, S. M., and van den Heever, S. C.: Aerosol-induced mechanisms for cumulus congestus growth. J. Geophys. Res.-Atmos., 120, 8941–8952, https://doi.org/10.1002/2015JD023743, 2015.

Sherburn, K. D., and Parker, M. D.: Climatology and ingredients of significant severe convection in high-shear, low-CAPE environments. Weather Forecast., 29, 854–877, https://doi.org/10.1175/WAF-D-13-00041.1, 2014.

Sherwood, S. C.: Aerosols and ice particle size in tropical cumulonimbus. J. Climate, 15, 1051–1063, https://doi.org/10.1175/1520-0442(2002)015<1051:AAIPSI>2.0.CO;2, 2002.

Smalley, K. M., and Rapp, A. D.: The role of cloud size and environmental moisture in shallow cumulus precipitation. J. Appl. Meteorol. Clim., 59, 535–550, https://doi.org/10.1175/JAMC-D-19-0145.1, 2020.

Sokolowsky, G. A., Freeman, S. W., and van den Heever, S. C.: Sensitivities of maritime tropical trimodal convection to aerosols and boundary layer static stability. J. Atmos. Sci., 79, 2549–2570, https://doi.org/10.1175/JAS-D-21-0260.1, 2022.

Spencer, R. W., Hood, R. E., Lafontaine, F. J., Smith, E. A., Platt, R., Galliano, J., Griffin, V. L., and Lobl, E.: High-resolution imaging of rain systems with the Advanced Microwave Precipitation Radiometer. J. Atmos. Ocean. Tech., 11, 849–857, https://doi.org/10.1175/1520-0426(1994)011<0849:HRIORS>2.0.CO;2, 1994.

Straka, J. M., Zrnić, D. S., and Ryzhkov, A. V.: Bulk hydrometeor classification and quantification using polarimetric radar data: Synthesis of relations. J. Appl. Meteorol., 39, 1341–1372, doi:10.1175/1520-0450(2000)039<1341:BHCAQU>2.0.CO;2, 2000.

Stroud, C. A., and Coauthors: Cloud activating properties of aerosol observed during CELTIC. J. Atmos. Sci., 64, 441–459, https://doi.org/10.1175/JAS3843.1, 2007.

van den Heever, S. C., and Cotton, W. R.: Urban aerosol impacts on downwind convective storms. J. Appl. Meteorol. Clim., 46, 828–850, https://doi.org/10.1175/JAM2492.1, 2007.

van den Heever, S. C., Carrió, G. G., Cotton, W. R., DeMott, P. J., and Prenni, A. J.: Impacts of nucleating aerosol on Florida storms. Part I: Mesoscale simulations. J. Atmos. Sci., 63, 1752–1775, https://doi.org/10.1175/JAS3713.1, 2006.

Varble, A. C., Igel, A. L., Morrison, H., Grabowski, W. W., and Lebo, Z. J.: Opinion: A critical evaluation of the evidence for aerosol invigoration of deep convection. Atmos. Chem. Phys., 23, 13791–13808, https://doi.org/10.5194/acp-23-13791-2023, 2023.

Veals, P. G., Varble, A. C., Russell, J. O. H., Hardin, J. C., and Zipser, E. J.: Indications of a decrease in the depth of deep convective cores with increasing aerosol concentration during the CACTI campaign. J. Atmos. Sci., 79, 705–722, https://doi.org/10.1175/JAS-D-21-0119.1, 2022.

Virtanen, P., and Coauthors: SciPy 1.0: Fundamental algorithms for scientific computing in Python. Nat Methods, 17, 261–272, https://doi.org/10.1038/s41592-019-0686-2, 2020.

Vömel, H., Goodstein, M., and Aredt, C.: Dropsonde data quality report: Clouds, Aerosol and Monsoon Processes-Philippines Experiment (CAMP2Ex, 2019). Version 1.0, UCAR/NCAR – Earth Observing Laboratory, https://www-air.larc.nasa.gov/cgi-bin/ArcView/camp2ex, accessed 16 November 2020.

Wang, J. K., Ford, T. W., and Quiring, S. M.: Distinguishing between unorganized and organized convection when examining land-atmosphere relationships. J. Appl. Meteorol. Clim., 54, 2229–2243, https://doi.org/10.1175/JAMC-D-15-0086.1, 2015.

Wentz, F. J., and Spencer, R. W.: SSM/I rain retrievals within a unified all-weather ocean algorithm. J. Atmos. Sci., 55, 1613–1627, https://doi.org/10.1175/1520-0469(1998)055<1613:SIRRWA>2.0.CO;2, 1998.

Wilheit, T. T., and Chang, A. T. C.: An algorithm for retrieval of ocean surface and atmospheric parameters from the observations of the scanning multichannel microwave radiometer. Radio Sci., 15, 525–544, https://doi.org/10.1029/RS015i003p00525, 1980.

Wilks, D. S.: *Statistical Methods in the Atmospheric Sciences*. Academic Press, 676 pp, ISBN 9780123850232, 2011.

Williams, E., and Renno, N.: An analysis of the conditional instability of the tropical atmosphere. Mon. Weather Rev., 121, 21–36, https://doi.org/10.1175/1520-0493(1993)121<0021:AAOTCI>2.0.CO;2, 1993.

Zhang, L., Rosenfeld, D., Pan, Z., Mao, F., Zhu Y., Lu, X., and Gong, W.: Observing aerosol primary convective invigoration and its meteorological feedback. Geophys. Res. Lett., 50, e2023GL104151, https://doi.org/10.1029/2023GL104151, 2023.